



UNIVERSITY OF LEEDS

This is a repository copy of *A review of tectonic, elastic and visco-elastic models exploring the deformation patterns throughout the eruption of Soufrière Hills volcano on Montserrat, West Indies.*

White Rose Research Online URL for this paper:

<https://eprints.whiterose.ac.uk/185017/>

Version: Accepted Version

Article:

Neuberg, JW orcid.org/0000-0001-7866-0736, Taisne, B, Burton, M et al. (4 more authors) (2022) A review of tectonic, elastic and visco-elastic models exploring the deformation patterns throughout the eruption of Soufrière Hills volcano on Montserrat, West Indies. *Journal of Volcanology and Geothermal Research*, 425. 107518. ISSN 0377-0273

<https://doi.org/10.1016/j.jvolgeores.2022.107518>

© 2022, Elsevier. This manuscript version is made available under the CC-BY-NC-ND 4.0 license <http://creativecommons.org/licenses/by-nc-nd/4.0/>.

Reuse

This article is distributed under the terms of the Creative Commons Attribution-NonCommercial-NoDerivs (CC BY-NC-ND) licence. This licence only allows you to download this work and share it with others as long as you credit the authors, but you can't change the article in any way or use it commercially. More information and the full terms of the licence here: <https://creativecommons.org/licenses/>

Takedown

If you consider content in White Rose Research Online to be in breach of UK law, please notify us by emailing eprints@whiterose.ac.uk including the URL of the record and the reason for the withdrawal request.



eprints@whiterose.ac.uk
<https://eprints.whiterose.ac.uk/>

1 **A review of tectonic, elastic and visco-elastic models exploring the deformation**
2 **patterns throughout the eruption of Soufrière Hills volcano on Montserrat, West Indies**

3

4 J.W. Neuberg¹, B. Taisne², M. Burton³, G. A. Ryan^{4,5}, E. Calder⁶, N. Fournier⁷, A.S.D.
5 Collinson¹

6 ¹ School of Earth and Environment, Leeds University, UK

7 ² Earth Observatory of Singapore, Nanyang Technological University, Singapore

8 ³ Department of Earth & Environmental Sciences, Manchester University, UK

9 ⁴ Montserrat Volcano Observatory, Flemmings, Montserrat, West Indies

10 ⁵ Seismic Research Centre, University of West Indies, Saint Augustine, Trinidad & Tobago

11 ⁶ School of GeoSciences, University of Edinburgh, UK

12 ⁷ GNS Science, New Zealand

13 **Abstract**

14 Since the eruption began in 1995, Soufrière Hills volcano on Montserrat has been
15 characterised by five phases of magma extrusion and corresponding pauses. Despite a lack
16 of eruptive surface activity since 2010, the volcano continues to show signs of unrest in the
17 form of ongoing outgassing, and inflation of the entire island of Montserrat. Using numerical
18 modelling, we compare a set of contrasting deformation models in an attempt to understand
19 the current state of Soufrière Hills volcano, and to gauge its future eruption potential. We
20 apply a suite of deformation models including faults and dykes, and an ellipsoidal source
21 geometry to all phases and pauses covering the entire eruptive history from 1995 through
22 2020. Based on recent petrological evidence suggesting no recent injection of magma from
23 depth after an initial magma intrusion, we test the hypothesis that the ongoing inflation of
24 Montserrat could be explained by a visco-elastic, crustal response to the initial magma

25 intrusion without a renewed pressurisation due to magma injection. In contrast to previous
26 modelling attempts, we focus on conceptual models and compare elastic- with several visco-
27 elastic models taking temperature-dependent viscosity models, tectonic components, mass
28 balance, magma compressibility and outgassing data into account. We explore a wide
29 parameter space in a Generalised Maxwell Rheology to explain the observed deformation
30 patterns, and demonstrate that a realistic, depth-dependent distribution of visco-elastic
31 parameters does not allow an interpretation of the deformation signal without any magma
32 influx or further pressurisation. Within the range of large uncertainties attached to the visco-
33 elastic model parameters we show that visco-elasticity reduces the degree of ongoing
34 pressurisation or magma influx into a crustal reservoir by a few percent. We conclude that
35 magma influx at a rate of 0.10 to 0.57 m³/s is the most likely explanation of the current
36 deformation pattern and is also in agreement with mass balance considerations and current
37 SO₂ flux observations.

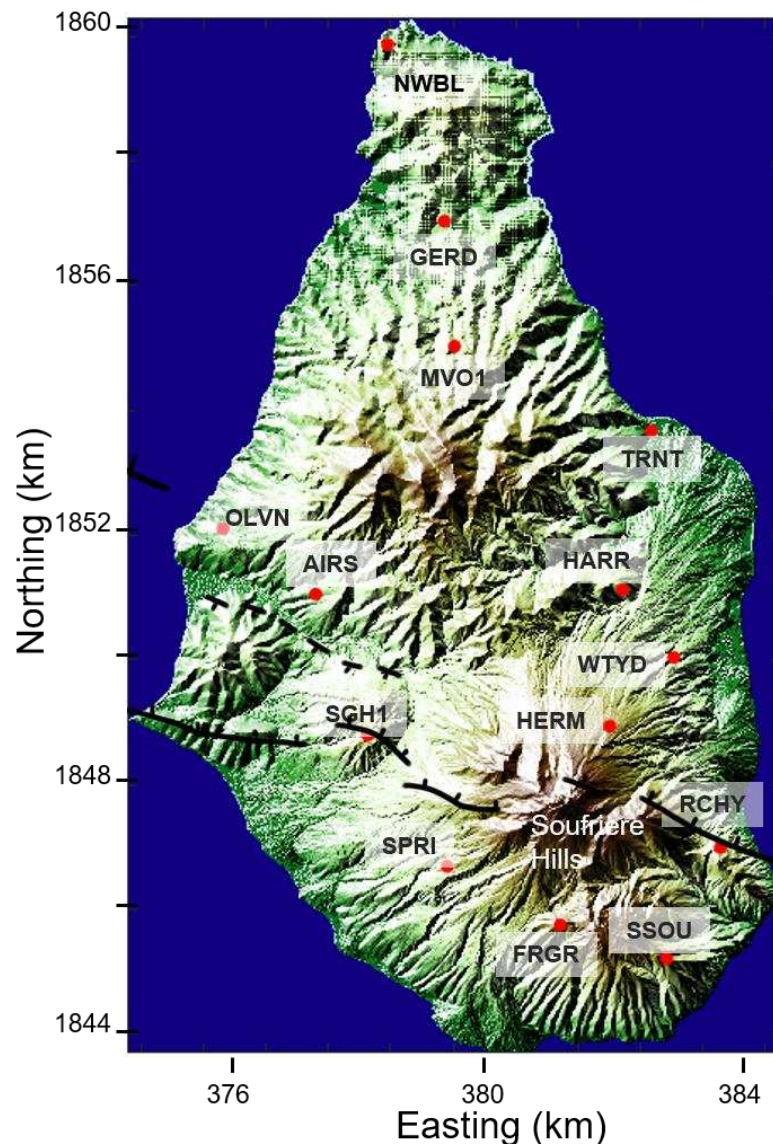
38 **Keywords:** Soufrière Hills, GPS, deformation, magma compressibility, Maxwell rheology,
39 visco-elastic response

40

41 **1. Introduction**

42 The current eruption of Soufrière Hills volcano (SHV), Montserrat (Fig.1), began in 1995, and
43 has been well documented in the literature (e.g. Kokelaar, 2002; Wadge et al., 2014). The
44 eruption has been characterised by five episodes of lava dome growth punctuated by dome
45 collapses, Vulcanian explosions, outgassing and ash venting (e.g. Edmonds et al., 2001,
46 2002; Watts et al., 2002; Hautmann et al., 2014). As depicted in Fig. 2, pauses of differing
47 duration have separated each phase such that despite lasting more than 25 years, the
48 volcano was only actively extruding for a total of 8.5 years (Wadge et al., 2014). The last
49 extrusive event recorded at the volcano on 11 February 2010, coincided with the partial
50 collapse of the northern section of the dome (Stinton et al., 2014). Since this event, the

51 volcano has entered a period of apparent quiescence with an average of 1.2 seismic events
52 per day (Stinton et al., 2014). By January 2022, Pause 5 has lasted for 12 years, significantly

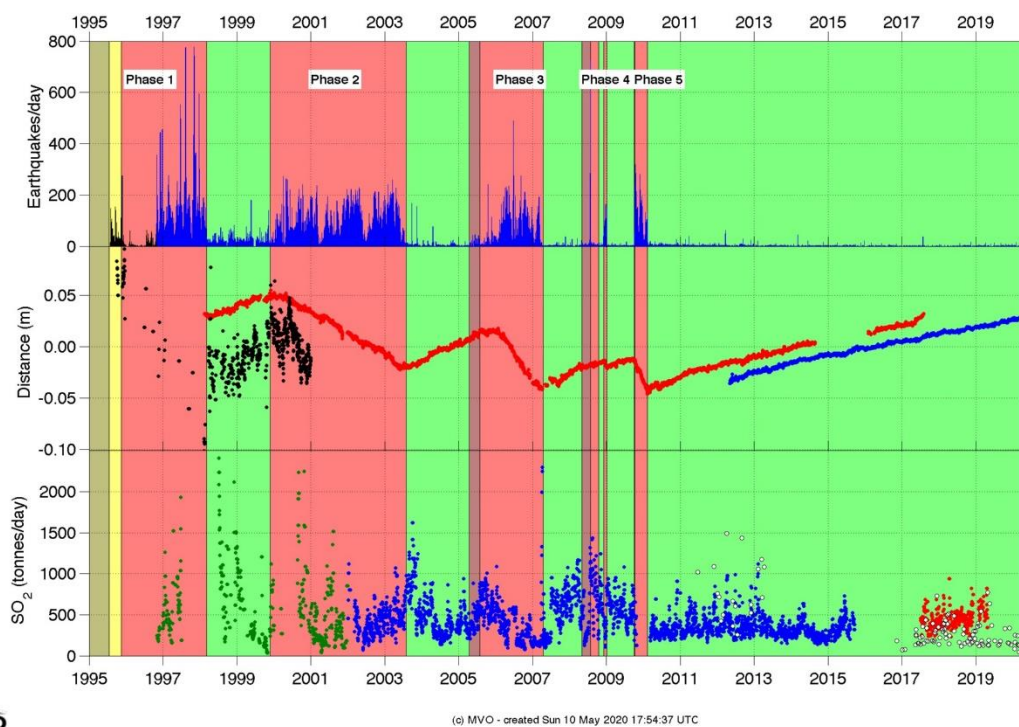


53
54 *Figure 1: Active Soufrière Hills volcano in the south of Montserrat; locations of major faults*
55 *(Feuillet et al., 2010) and cGPS stations used in this study.*

56 longer than any other pause, the immediate implication being that it is a pause - not the end
57 of the eruption. A mean daily SO₂ flux of approximately 200 tonnes/day (Stinton et al., 2020),
58 recorded until April 2020, and ongoing inflation of the island, continuously monitored by
59 cGPS (Fig. 2), are indications of ongoing volcanic unrest. Due to the lack of a monitoring
60 baseline for the background activity of Soufrière Hills, the question remains as to whether

61 these signals indicate potential future extrusive activity, or if the eruption can finally be
62 declared over.

63 Throughout the history of the eruption, there have been many attempts to determine the
64 configuration of the SHV plumbing system summarised in Elsworth et al.(2014). Deformation
65 models fall into two broad categories - either vertically-stacked magma reservoirs (Elsworth
66 et al., 2008, 2014; Foroozan et al., 2010, 2011; Hautmann et al., 2010) or single, vertically-
67 extended sources (Voight et al., 2010). The source geometries range from spheres to
68 prolate or oblate ellipsoids with rotational symmetry, which results for some studies in the
69 necessity for partial or complete omission of certain GPS stations in order to match model
70 output and GPS data (e.g. Hautmann et al., 2010; Foroozan et al., 2011).



71

72 *Figure 2: Monitoring data for the entire duration of the ongoing eruption at Soufrière Hills*
73 *volcano with the number of seismic events per day (top), vertical displacement for HARR*
74 *(black) and radial ground motion of MVO1 (red) and NWBL (blue) relative to the dome centre*
75 *(middle). SO₂ daily flux (bottom) monitored with different methods: COSPEC (green),*
76 *scanning DOAS (blue /red), traverse DOAS (white). Despite its prolonged duration, Pause 5*

77 *is characterised by ongoing SO₂ outgassing and surface deformation, but limited seismicity.*
78 *Adopted from Stinton et al., (2020).*

79 In contrast to attempting a detailed, perfect match of deformation data recorded on all
80 stations of the continuous GPS network (cGPS), we employ an entire suite of contrasting,
81 numerical models and focus on their conceptual differences. We aim at answering the critical
82 question whether the eruption is continuing or not. We follow the conceptual models that
83 have been guiding the discussions of the Scientific Advisory Committee on Montserrat
84 Volcanic Activity throughout the eruption. These models range from magma extrusion and
85 reservoir refill, to the influence of tectonic effects, potential contributions of crystallisation to
86 the pressurisation of the system, to the final end-member model of a visco-elastic response
87 to a major intrusion that has actually ceased several years ago.

88 We start with a purely elastic model to determine the source geometry of a deformation
89 source which can match the deformation data for Pause 5. In order to explore processes
90 alternative to magma influx explaining the ongoing inflation during Pause 5, we also address
91 the potential contributions of local tectonics such as the WNW- trending Belham Valley fault,
92 part of the Montserrat-Bouillante fault system (Feuillet et al., 2010) which is related to the
93 wider regional tectonics of the Northern Lesser Antilles section of the Caribbean plate with a
94 North-South extension (Wadge et al., 2014). We then adopt the geometry of a central,
95 elliptical source to model the dominant patterns of all eruptive phases and pauses, as well as
96 its anisotropic nature. By considering magma compressibility and extruded volume, we
97 estimate the respective volume changes for all phases and pauses throughout the eruption.
98 In this step, we interpret the iconic saw-tooth pattern in the deformation data (Fig. 1) as
99 erupted and re-charged material, respectively. Given recent petrological evidence (McGee et
100 al., 2019) which suggested that the intrusion of mafic magma had ceased by 2004, we
101 employ a set of visco-elastic models based on a temperature-dependent Maxwell rheology,
102 and test the alternative hypothesis that the observed saw-tooth deformation pattern can be
103 explained without any further magma influx.

104 **2. Continuous GPS data**

105 The cGPS network on Montserrat comprises 14 stations distributed across the island (Fig.
106 1). The data used for our initial analysis of Pause 5 covered a time period of 3 years from
107 August 2012 – July 2015, which presents a sufficiently long time interval after the previous
108 eruptive activity of February 2010, and a short ash-venting episode that occurred in March
109 2012, in order to focus on the underlying deformation trend. The velocity of each station has
110 been calculated relative to the motion of the Caribbean Plate using the GAMIT/GLOBK tool
111 suite (Herring et al., 2010a, 2010b). The plate motion has been defined by a number of
112 stations and the averaged displacements for the 2012 – 2015 period were derived from
113 these velocities.

114 Due to the short durations of Phases 4, 5 and Pause 4, and the requirement for a data
115 coverage of at least one-year for a sufficiently accurate deformation estimate, we omit these
116 stages from the following comparison depicted in Fig. 3. When normalised relative to the
117 station HARR, which is a station with data available for the entire eruptive history, there is a
118 remarkable similarity in relative magnitude of the horizontal, and, to a lesser extent, of the
119 vertical velocities across the stations for all stages of the eruption. The relative horizontal
120 magnitudes are the same, both for the eruptive phases and pauses. With the vertical
121 displacements being inherently noisier than the horizontal components, we assume that the
122 displacement rate can be caused by the same source geometry throughout the eruption
123 since it began in 1995. Furthermore, this highlights the repetitiveness of the source process,
124 for both apparent inflation and deflation, affecting all but the closest stations with the only
125 difference being the overall magnitude of displacement rate.

126 In agreement with the other pauses (e.g. Hautmann et al., 2010; Voight et al., 2010;
127 Foroozan et al., 2011), the majority of the cGPS stations showed a displacement away from
128 the volcano that increases with distance (Fig. 4 and 5). We assume the region to the south
129 of the volcano would show a similar displacement pattern to that in the north, but due to the
130 limited size of the island, and the location of the volcano in the south, this can be neither

131 corroborated nor invalidated. The three closest cGPS stations to the volcano (HERM, SPRI
132 and FRGR) deviate from this pattern by recording motion towards it. This is different to the
133 other pauses in the eruption history and may indicate a deviation of some processes
134 affecting these proximal stations which will be further discussed below.

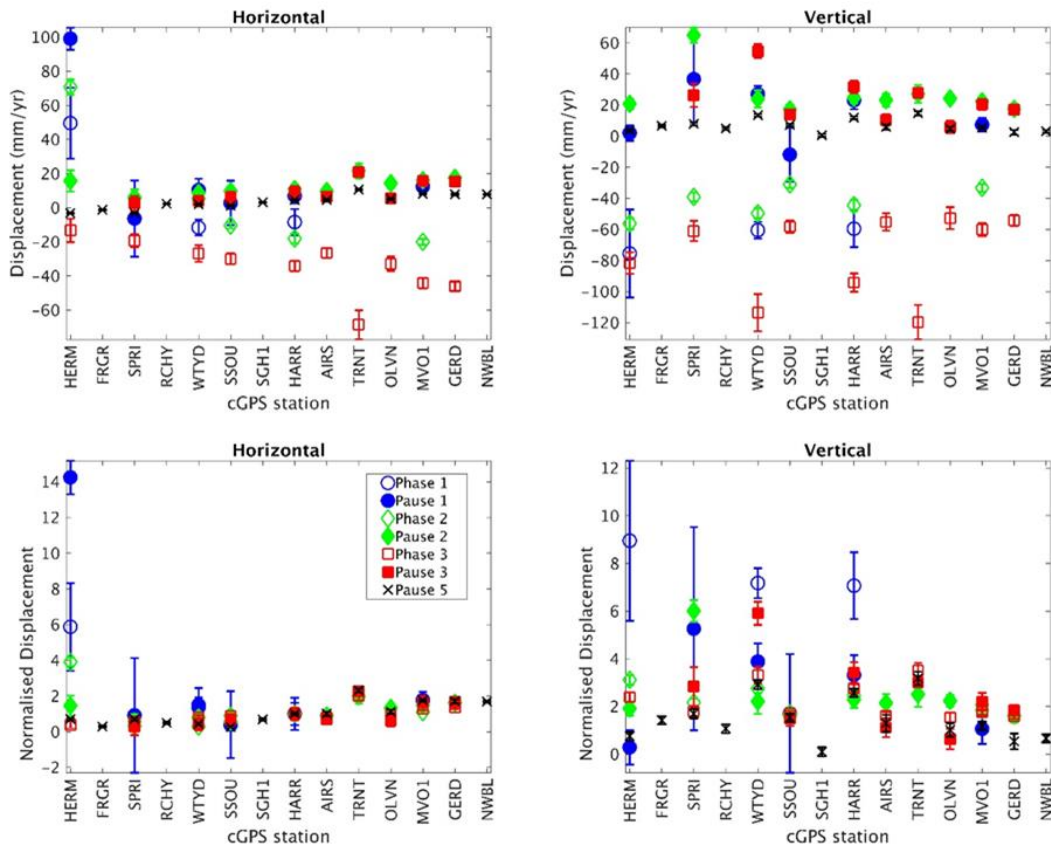
135 The characteristic deformation patterns that guide our modelling approach are the increasing
136 deflation rates for consecutive phases, in contrast to the decreasing inflation rates for
137 pauses, and the sharp transitions between pauses and phases as depicted in Fig. 2.

138 **3. Numerical Modelling**

139 To determine the configuration of sources required to replicate the current displacement
140 pattern on Montserrat, we have created a set of numerical models using Comsol
141 Multiphysics 5.4, which utilises a finite element method. Simple models have been calibrated
142 against analytical solutions (e.g. Mogi, 1958; Okada, 1985, 1992; McTigue, 1987; Del Negro
143 et al., 2009), and have been used to assess the potential contribution of several source
144 types such as a tectonic (strike-slip) versus a volume source (dyke or spherical chamber).
145 Because the study area is small (< 10km) compared to its distance to the subduction zone (>
146 200 km), vertical displacements due to vertical plate motion would be similar (i.e., within the
147 uncertainty on daily positions) at all stations in Montserrat. We therefore assume that
148 observed vertical deformation variations across the network are caused by local, plate-
149 internal tectonics or magmatic sources. We have systematically modified the location, size
150 and orientation of each source type to achieve the optimum match to the data. Finally, once
151 the source type has been established, source parameters have been further refined to
152 optimise the match to the data.

153 The model geometry has been created with a central block with dimensions of 12 km x 18
154 km x 50 km, embedded in a larger block of lateral extent 300 km x 300 km and depth 50 km.
155 Into this framework, we have inserted a variety of different source types and configurations.
156 Volume sources have been modelled using spherical or elliptical geometries whereas

157 tectonic fault movements have been modelled as finite planar surfaces. For spherical and
 158 elliptical magmatic sources, we have imposed pressure as boundary conditions; for dykes
 159 and faults we have employed displacement. We have modelled the elastic crust as either
 160 homogeneous with a Young's modulus of 10 GPa (e.g. Elsworth et al., 2014) and a



161
 162 *Figure 3: Horizontal and vertical displacement rates for Phases (1-3) and Pauses (1-3, 5)*
 163 *(top) in order of increasing distance from the volcanic edifice. All data are normalised relative*
 164 *to the horizontal displacement at HARR (bottom). A negative horizontal displacement*
 165 *represents motion towards the volcano. Therefore, the displacement direction is generally*
 166 *towards the volcano during phases and away from it during pauses. For the normalised*
 167 *horizontal cGPS data, all stations except HERM are in good agreement indicating an*
 168 *identical source geometry throughout the eruption. The discrepancy with HERM may be due*
 169 *to the proximity to the volcano, and a greater sensitivity to shallow conduit/dome processes.*
 170 *Phase 1 – Pause 3 data adapted from Mattioli et al. (2010) and Foroozan et al. (2011). No*
 171 *data plotted for Phase 4 – 5 due to their limited duration.*

172 Poisson's ratio of 0.25, or later in Section 5.4, have employed a depth-dependent model
173 based on seismic tomography (Paulatto, 2011; Paulatto et al., 2019) where correction
174 factors of 0.67 to 0.11 have been applied to account for the difference in elastic behaviour
175 between short-period seismic time scales and long-period, static deformation
176 (Gudmundsson, 1990). For the visco-elastic models we have used the same source
177 geometry and average viscosities in the range between 10^{18} and 10^{19} Pas, and later
178 temperature/depth-dependent viscosity distributions derived from different temperature
179 models according to the Arrhenius approximation. We used roller boundary conditions at the
180 sides, fixed conditions at the bottom, and a free surface at the top. The finite element mesh
181 comprising tetrahedral elements of varying sizes consists of up to 100,000 elements
182 resulting in 4 million degrees of freedom.

183 **4. Modelling results**

184 Initially, our modelling attempts have focussed on data from Pause 5, which has the best
185 data coverage and shows the most consistent long-term trend. After finding the model
186 geometry that best matches the data set, we have applied the same source type to previous
187 eruptive phases and pauses.

188 **4.1. Effect of topography**

189 Previous studies have often assumed a flat surface to their models, stating topography has
190 little effect on the surface displacement pattern for deep sources (e.g. Hautmann et al.
191 2010). Marsden et al. (2019) have demonstrated that, to some extent, this is true for
192 isotropic sources, but it is not applicable for more complex sources. They found a significant
193 difference close to the volcanic edifice, where high dome topography affects both the
194 magnitude of surface displacement and its direction, which may be completely reversed
195 (Marsden et al., 2019). However, regarding the main objective of this study, the influence of
196 topography does not play an important role to find the principle causes behind the ongoing,
197 island-wide inflation.

198 **4.2. Basic source models: dyke, fault and their combination**

199 Our overall modelling strategy is led by the aim to explore source models alternative to
 200 previous studies that were based on pressurising deep magma reservoirs. There is
 201 significant evidence for previous tectonic activity in the vicinity of the island, in particular the

Model Reference	Topography	Crustal Response	Description Source	Parameter Final/Range	Stations used
I_S	y	elastic	expanding sphere	radius 1 [0.5, 2] km depth 6 [1, 10] km expansion 0.25 m	all cGPS
I_D	y		expanding dyke	dimension 5 x 1 km expansion 1 m azimuth 263° [200°,300°]	
I_F	y		sinistral fault	dimension 5 x 1 km strike-slip 1 m azimuth 293° [280°,300°]	
E_{1E}	y		expanding ellipsoid	0.6 x 0.6 x 2.0 km depth 6 [1, 10] km azimuth 263°	
E_{2E}	y		two expanding/ contracting ellipsoids	0.6 x 0.6 x 2.0 km depth 6 [1, 10] km azimuth 263° 0.3 x 0.3 x 1.0 km depth 0 [0, 3] km azimuth 293°	
E_{2Ex}	y		two expanding/ contracting ellipsoids with depth extension	0.6 x 0.6 x 2.0 km depth 6 [1, 10] km azimuth 263° 0.3 x 0.3 x 1.0 km depth 0 [0, 3] km azimuth 293° depth extension 8 [0, 20] km pressure (10, 2.5] MPa/year	
E_{1Ex}	y		expanding single ellipsoid with depth extension	0.6 x 0.6 x 2.0 km depth 6 [1, 10] km azimuth 263° depth extension 8 [0, 20] km pressure [10,2.5] MPa/year	
V_H	n	visco-elastic Maxwell homogeneous		source as above viscosity [1.8, 12] x10 ¹⁸ Pas Youngs mod [5, 10] GPa	MVO1 TRNT
VZ_{Max}	n	visco-elastic Maxwell depth-dep.		Maxwell rheology: depth-dependent temperature, viscosity, elasticity see Fig. 13/14. E(z) reduced to 11 & 67% pressure/volume see Tab 3	
VZ_{SLS}	n	visco-elastic SLS depth-dep		SLS rheology: depth-dependent temperature, viscosity, elasticity see Fig. 13/14. E(z) reduced to 11 & 67% pressure/volume see Tab 3	

202

203 *Table 1: Summary of numerical models employed throughout this study.*

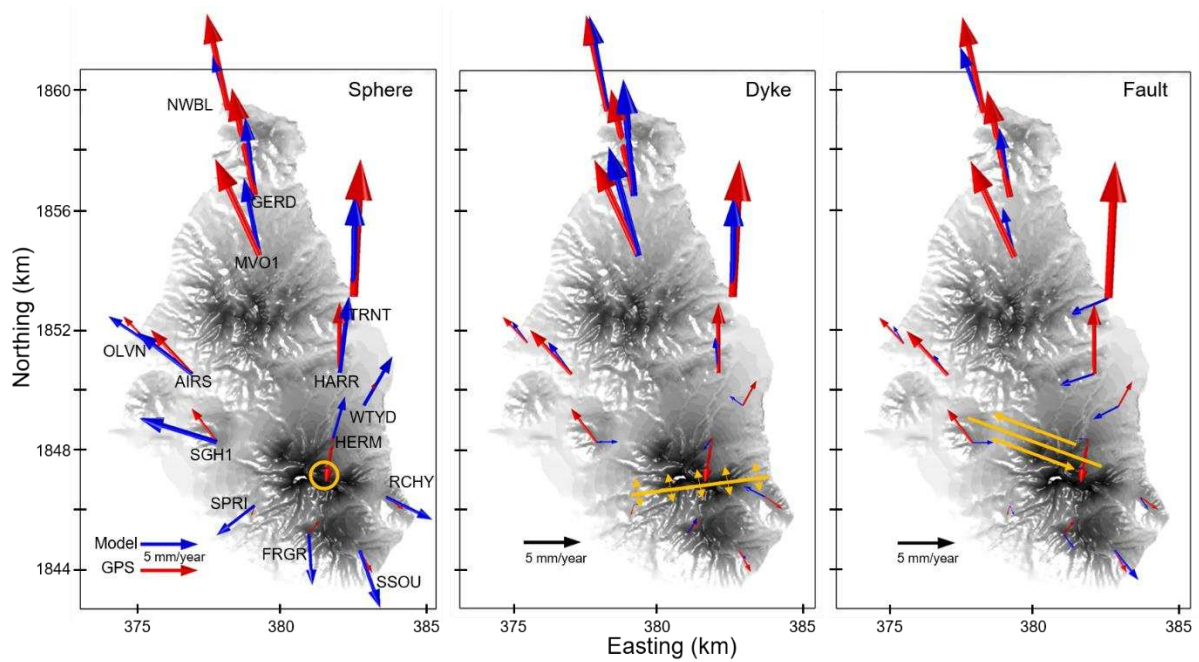
204 presence of faults crossing the island, including the Montserrat-Havers Fault, the Belham
205 valley Fault and the Richmond Hill Fault (Fig.1) contributing to the Montserrat-Bouillante
206 Fault System (Feuillet et al., 2010). A regional GPS study by Lopez et al. (2006) indicates a
207 small N-S intraplate extension in the area of the Lesser Antilles where Montserrat lies. The
208 NNW trans-tensional fault system between Montserrat and Guadeloupe is thought to
209 accommodate some of this extension. We approximate this tectonic extension as a NW-SE
210 extension of the exterior northern and southern model boundaries. For example, a NW-SE
211 extension of 10 mm/year at 25 km distance from the Belham Valley, in each direction, would
212 result in an on-island extension of 2.5 mm/year.

213 Hence, the first set of models comprises strike-slip faults and expanding dykes (Fig. 4) which
214 are employed individually with a simple sphere for comparison. For each source type, the
215 depth of the top has been varied at 0.5 km intervals between 1-10 km below sea level
216 (b.s.l.), for different vertical and horizontal extents, lateral positions and strike directions.

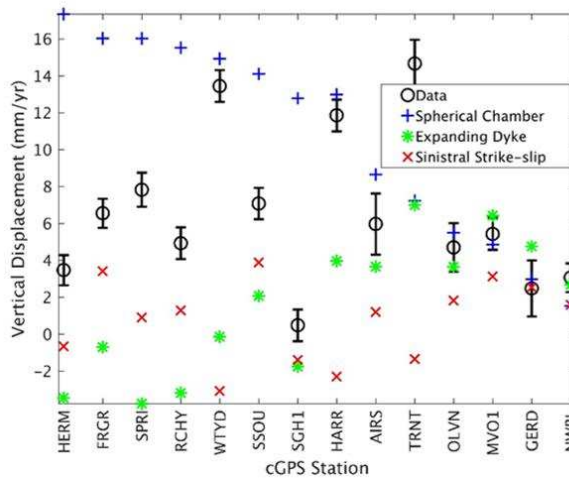
217 Fig. 4 shows best-fit results for each of the three basic source models. The spherical magma
218 chamber (Model I_S) has an initial radius of 1 km, centred at 6 km b.s.l. and has been
219 modelled with a pressure of 4 MPa resulting in a uniform radius increase by 0.25 m. The
220 initial dyke (Model I_D) and strike-slip (Model I_F) sources both have dimensions of 5 km x 1 km
221 x 1 m to which we have applied displacement boundary conditions of 0.5 m in each direction.
222 The dyke depicted in Fig. 4 has been modelled with an orientation of 263° whilst the sinistral
223 strike-slip motion has been simulated with a fault striking at 293°.

224 The results of the simple strike-slip sources show a bad match to the data, and using a
225 WNW-trending orientation, parallel to the Belham Valley (Wadge et al., 2014), they only
226 match the stations furthest north. In contrast, the expanding spherical and dyke sources both
227 show a better match. However, unlike the spherical source model, an expanding dyke
228 source (I_D) satisfies both, the non-rotationally symmetric nature of the data, as well as the
229 requirement for an increased horizontal displacement with distance from the volcano. Due to

230 the observed surface displacement pattern, characterised by increased horizontal
 231 displacement



232



233

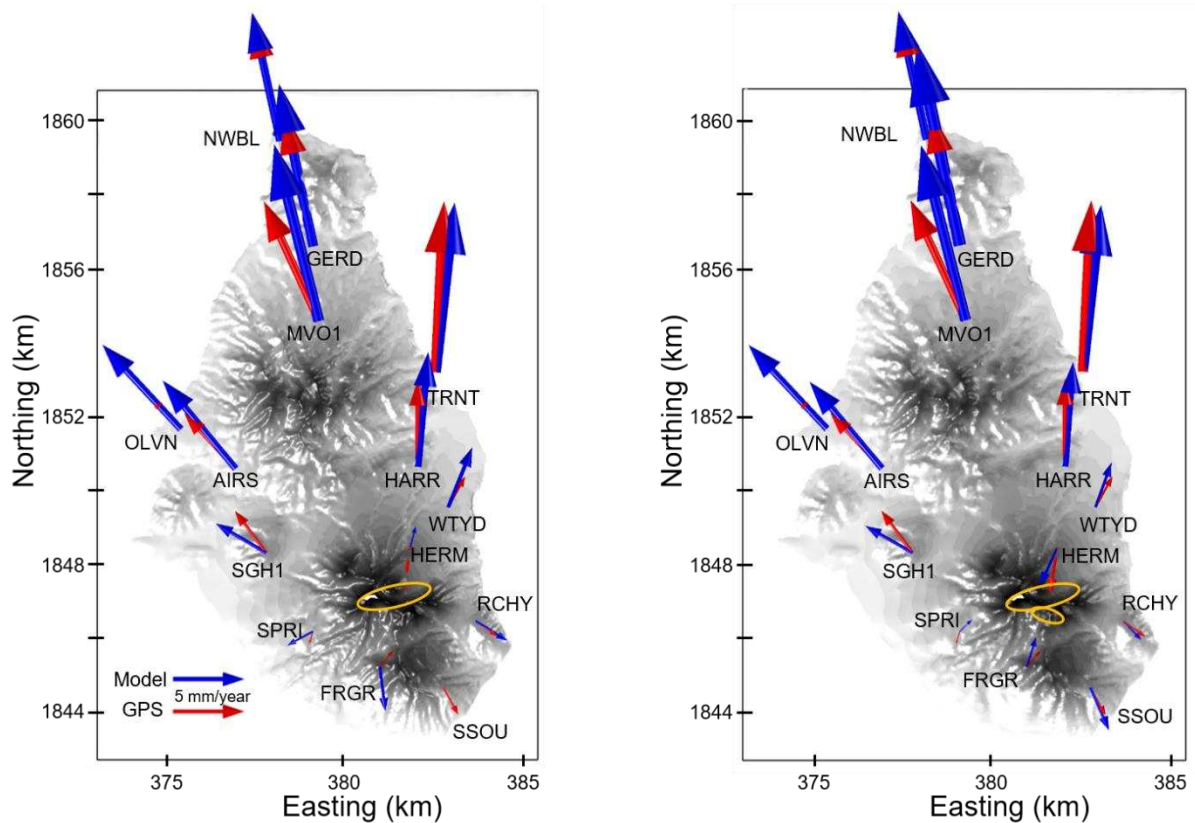
234 *Figure 4: Horizontal (top) and vertical displacement rates (bottom) for basic source models,*
 235 *fitting spherical reservoir, dyke and sinistral strike-slip. The stations are listed in order of*
 236 *increasing horizontal distance from the volcano. High resolution topography is included and*
 237 *the location and orientation of the sources are marked on the maps. For both the horizontal*
 238 *and vertical component of the displacement, the expanding dyke (1b) shows the closest*
 239 *match to the Pause 5 data.*

240

241 away from the volcano and a north-south trend, we discount rotationally symmetric sources,
242 or their combinations, and sources located at less than 4 km depth. The mismatch with the
243 GPS data in Fig. 4 is evident and results in an absolute data misfit of 28.1 mm for the dyke
244 model I_D , 53.5 mm for the fault model I_F , and 43.2 mm for the spherical model I_S . Hence, we
245 conclude that none of these three source types (I_S , I_D , and I_F) match the deformation data of
246 Pause 5.

247 **4.3. Initial volume models**

248 After disregarding the basic source models (I_S , I_D , and I_F) in the previous section as
249 alternatives to continued magma influx, we return to volume-based sources, however
250 employing now non-rotationally symmetries. We adopt the spherical source centred at 6 km
251 depth and transform it into an expanding ellipsoid by varying the half axes and orientation
252 systematically (Table 1) deriving at a geometry of semi-axes 1 km x 0.3 km x 1 km, volume
253 1.26 km^3 , centred at 6 km b.s.l. and orientation of 263° (Model E_{1E}). This source model
254 matches the observation of the distal GPS stations better than any rotationally symmetric
255 source (Fig. 5, left). In order to include the data observed on the close GPS stations, a
256 second, shallow deflating ellipsoidal source (Model E_{2E}) of semi-axes 500 m x 150 m x 150
257 m, volume 0.05 km^3 , centred at sea level and an orientation of 293° (Fig. 5, right). The
258 corresponding data misfits are 26.1 mm and 18.4 mm for models E_{1E} and E_{2E} , respectively.
259 We refer to this set of volume sources as 'Initial Elastic Models' (see Tab.1: E_{1E} , E_{2E} , and
260 E_{1Ex}) and use them to explore in the following sections their compatibility with previous
261 pauses and phases, their potential trade-off with depth, the impact of magma
262 compressibility, and finally the potential impact of a visco-elastic crust in which these volume
263 sources are embedded. All these strands of investigation focus on better quantifying the
264 processes that cause the island – wide inflation of Montserrat or aim to find alternative
265 explanations.



267

268 *Figure 5: Horizontal displacement rates (blue) for the 'Initial Elastic Models' E_{1E} and E_{2E}*
 269 *compared to the Pause 5 data (red). Source geometry (yellow) is projected onto the surface.*
 270 *Left: only deep source is modelled E_{1E} . Right: dual source of deep and shallow ellipsoids are*
 271 *used E_{2E} (see text). Note, the shallow source affects only the stations HERM, SPRI and*
 272 *FRGR close to the volcano.*

273 Assuming a homogeneous medium, Young's modulus of 10 GPa, and a Poisson's ratio of
 274 0.25, a uniform inflation of 10 MPa per year for the deep source and deflation of 5 MPa per
 275 year for the shallow source is required to explain the surface deformation. Equivalent volume
 276 changes related to inflation and deflation are determined through eq. 1-5 in the next section
 277 and expressed as volume change rates by considering a time span of 10 years in Pause 5.
 278 Hence, 10 MPa/year and 5 MPa/year correspond to a uniform source volume change rate of
 279 $0.05 \text{ m}^3/\text{s}$ and $0.003 \text{ m}^3/\text{s}$ for the expanding deep source and contracting shallow source,
 280 respectively (Model E_{2E}).

281 **4.4 Volume - pressure equivalence**

282 Surface deformation due to a magmatic intrusion has been often modelled by a Mogi source
283 (Mogi, 1958) where the intrusion is represented by a small, spherical cavity of radius a ,
284 embedded in an elastic half space at depth d . An isotropic stress is applied to the cavity wall
285 which corresponds to the overpressure P exerted by the intrusion. The deformation at the
286 stress-free surface is calculated in an iterative approach leading to a point source
287 approximation ($a \ll d$) which is satisfied if $a < \frac{1}{2} d$.

288 The corresponding volume change ΔV in the cavity can be approximated for a spherical
289 geometry in an isotropically elastic half space by (McTigue, 1987)

290
$$\Delta V \approx \pi P a^3 / \mu \quad (1)$$

291 with the shear modulus

292
$$\mu = \frac{E}{2(1 + \nu)}, \quad (2)$$

293 Young's modulus E , and Poisson's ratio ν .

294 For a Poisson's ratio of $\nu = \frac{1}{4}$ this leads to a relative volume change

296
$$\frac{\Delta V}{V} = \frac{3}{4\mu} P \quad (3)$$

295 or

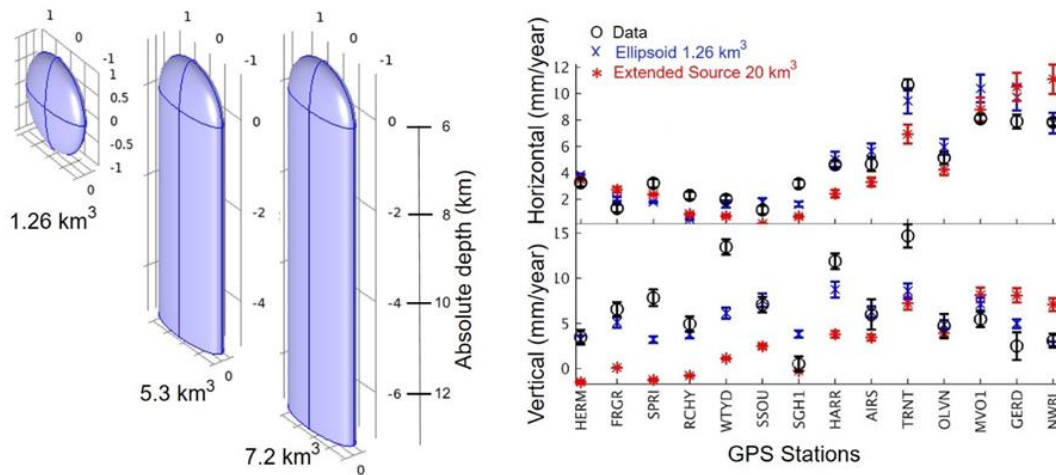
297
$$\frac{\Delta V}{V} = 1.875 \frac{P}{E}. \quad (4)$$

298 For geometries used in our models (Models E_{1EX}, Fig. 6) we have used an equivalent
299 expression

300
$$\frac{\Delta V}{V} = k \frac{P}{E}, \quad (5)$$

301 where k has been determined by numerical integration over the volumetric strain along the
302 source geometry. For an ellipsoid $k = 3.5$, and for a depth-extended elliptical source

303 geometry reaching a depth of 12 km and 14 km, $k = 4.8$ and $k = 5$, respectively. This allows
 304 us to convert pressure changes of different source geometries into equivalent volume
 305 changes of incompressible magma in a cavity embedded in an elastic half space as seen in
 306 the following section (Fig. 6 and 7).



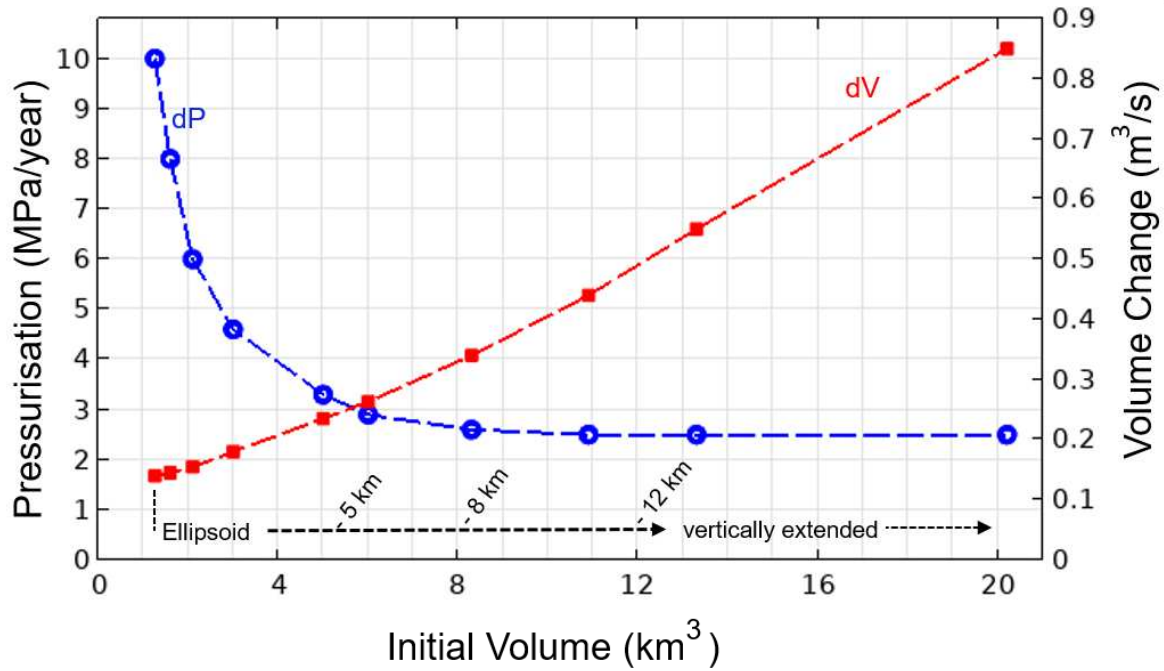
307

308 *Figure 6: Left, source geometry (E_{1Ex}): elliptical cross section 600m x 2000m; shown for*
 309 *depth range of vertically extended geometry by 5,000 m and 7,000 m, or total depth to*
 310 *11,000 m and 13,000 m. Right: Impact of modelled vertically extended volume to the vertical*
 311 *and horizontal displacement of the Pause 5 data. The stations are listed in order of*
 312 *increasing horizontal distance from the volcano. Model results are illustrated for the initial*
 313 *ellipsoidal model with 10 MPa pressure and a source extended vertically up to 20 km³ with a*
 314 *pressure of 3 MPa. The shallow deflating source remains the same for both models (Model*
 315 *E_{2Ex}). Using a large initial volume results in a large relative surface displacement at the more*
 316 *distal stations (MVO1, GERD, NWBL).*

317 4.5. Constraints on source volume and model trade-offs

318 Following the study by Christopher et al. (2015) that points to a larger magma reservoir
 319 under Montserrat, we have explored the parameter space by adding to our magmatic source
 320 at 6 km depth a deeper root (Model E_{2Ex}). We have increased the volume by extending it
 321 vertically through an insertion of additional volume below the upper hemisphere of the

322 elliptical source geometry, as depicted in Fig. 5. This maintains the shape of the top of the
 323 source controlling most of the closer surface deformation, but increases the depth to which
 324 the source can be pressurised, relevant for distal stations.



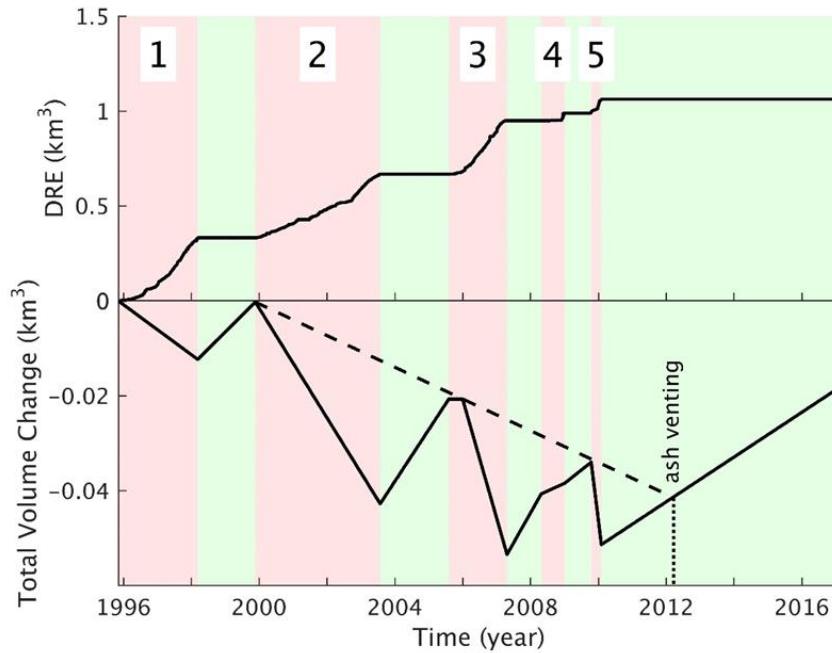
325
 326 *Figure 7: Annual pressure increase (dP, blue) applied to the extended sources as shown in*
 327 *Fig. 6, and resulting volume change (dV, red) against initial volume. The pressure required*
 328 *to match the data converges to 2.5 MPa for sources extended to a volume in excess of 8*
 329 *km³. All data points (i.e. combinations of pressure increase and initial volume; blue dots)*
 330 *result in a similarly good data match. Increasing the initial volume beyond 8 km³ yields a*
 331 *linear increase in volume change, while the equivalent annual pressure increase remains*
 332 *constant.*

333 When extending the source vertically and reducing the pressure simultaneously we maintain
 334 an equally good match to the horizontal, distal GPS data, and an interesting pattern arises
 335 (Fig. 7): Once the source is extended vertically to a depth of 14 km and a total initial volume
 336 of about 8 km³, the pressure increase required to match the Pause 5 data converges at
 337 about 2.5 MPa/year. This indicates a trade-off between source pressure and initial volume of

338 a magma reservoir into which new magma could enter. The bigger this initial volume, the
339 larger is the volume of magma influx, creating the same pressure increase and,
340 consequently, the same deformation field. Hence, the estimate for a corresponding magma
341 influx can vary from 0.14 m³/s for an initial reservoir volume only 1.25 km³ (ellipsoidal
342 geometry in our initial model E_{1E}) to 0.85 m³/s for a reservoir (E_{1Ex}) of about 20 km³ (Fig.7 –
343 right hand axis). Assuming magma accumulation into a larger, initial reservoir as the only
344 source process provides an upper bound of equivalent pressurisation of about 2.5 MPa/year.
345 In general, this attempt to explore the depth – pressure trade-off also demonstrates why
346 many other studies have used vertically extended ellipsoids in their models (Elsworth et al.,
347 2014), and confirms the fact that geodetic data are not sensitive to vertical extensions of
348 magma reservoirs.

349 **4.6. Application to previous phases and pauses and impact of magma compressibility**

350 Following Fig. 3, there is a remarkable similarity in displacement patterns between all the
351 pauses and phases recorded at SHV. Using the initial model (E_{1E}) defined in 4.3, we go
352 backwards in time and model the deflation during eruptive Phase 3, which can be matched
353 by a depressurisation of about 40 MPa or a corresponding volume change of 17 x 10⁶ m³ at
354 the deep source. The modelled volume changes for all phases and pauses until 2017 are
355 summarised in Fig. 8, together with the estimated dense rock equivalent (DRE) volumes
356 according to Wadge et al. (2014). Consequently, we can assume that the general source
357 geometry must have remained stable through time with the GPS network measuring
358 significant variations in magma volume or pressure. Note that there is a large discrepancy
359 between modelled volume change at depth and estimated dense rock equivalent which can
360 be accounted for by introducing a compressible magma at depth.



361

362 *Figure 8: Cumulative DRE volume erupted (adapted from Wadge et al., 2014) (top) and the*
 363 *change in total source volume through time relative to the start of the eruption (bottom).*

364 *Total source volume change is based on the initial elliptical source volume (Model E_{1E}) of*
 365 *1.26 km³. The dashed line indicates the trend of eruption onsets for Phases 2, 3 and 5. The*
 366 *location of the March 2012 ash-venting event is indicated.*

367 A negative or positive volume change within the source model corresponds directly to
 368 extruded or intruded incompressible magma from, or into a reservoir, respectively. However,
 369 due to its volatile content, magma is compressible which leads to discrepancies when
 370 comparing DRE of extruded material with pressure or volume changes at depth as indicated
 371 in Fig. 8. In order to reconcile this discrepancy between apparent volume change at depth
 372 derived from modelling the deformation field, and the erupted volume (DRE) during eruptive
 373 phases we have to consider the compressibility of magma at depth. The change in volume
 374 within the source region (V_M) can be linked to the estimated DRE volume (V_{DRE}) by applying
 375 conservation of mass (Segall, 2010)

379
$$\delta V_M = \delta V_{DRE} \left(\frac{\rho_{DRE}}{\rho_M} \right) \left(\frac{1}{1 + \frac{\beta_M}{\beta_s}} \right), \quad (6)$$

376 where the DRE density (ρ_{DRE}) is 2600 kg/m³ (Wadge et al., 2010), while β_s and β_M are the
 377 compressibility of source reservoir and magma, respectively (Table 2). The magma source
 378 density (ρ_M) has been calculated according to

380
$$\rho_M = \left[\frac{n}{\rho_g} + (1 - n) \left(\frac{x}{\rho_c} + \frac{1 - x}{\rho_m} \right) \right]^{-1} \quad (7)$$

381 (e.g. Huppert & Woods, 2002; Neuberg & O’Gorman, 2002). All variables have been defined
 382 in Table 2. Assuming water as the main volatile phase, we have used Henry’s law of
 383 solubility to calculate the exsolved water content ($n = N - 4.11 \times 10^{-6} \sqrt{P}$), the gas density
 384 following the ideal gas law ($\rho_g = MP/RT$) with a total volatile content (N) of 4 - 6 wt.% and
 385 crystal content (x) of 40% (Huppert & Woods, 2002). Edmonds et al. (2014) consider a
 386 larger total volatile content, however, with 6 wt% we take into account the effects of
 387 continued outgassing. The compressibility of the source magma (β_M) and magma reservoir
 388 (β_c) have been calculated as (e.g. Segall, 2010)

389
$$\beta_M = \frac{1}{\rho_M} \frac{\partial \rho_M}{\partial P} \quad \text{and} \quad \beta_c = \frac{1}{V_M} \frac{\partial V_M}{\partial P}, \quad (8)$$

390 respectively, and will be used in the following sections whenever magma at depth is being
 391 compared with DRE.

392 **4.7 Summary of elastic models**

393 Fig. 5 depicts a reasonable match between data and our models E_{1E} and E_{2E} based on a
 394 homogeneous, elastic crust below the Montserrat topography. Maintaining the shallow
 395 ellipsoidal source (E_{2E}) is needed to force the horizontal displacement of the three close
 396 stations to point inwards. The vertical displacements are less well fitted when we use
 397 vertically extended sources as those can result in a trade-off between horizontal and vertical
 398 displacement. A classic example is the displacement field of a dyke that results in a negative

399 vertical displacement above the dyke which increases with the amount of dyke opening while
400 a positive horizontal displacement prevails in the far field. Dieterich & Decker (1975) have
401 demonstrated that, in order to constrain the source geometry perfectly, both horizontal and
402 vertical components are needed, however this is not the aim of this study. By introducing
403 more model parameters, either by refining the geometry or by introducing a two- or even
404 three-dimensional elastic model the data fit could be further improved. This has been
405 achieved by several previous studies which were all based on an elastic response to magma
406 influx or drainage (e.g. Elsworth et al., 2008; Hautmann et al., 2010; Foroozan et al., 2011).
407 Our attempt to explore the depth – pressure trade-off in Section 4.5 demonstrates why many
408 other studies have used prolate spheroids in their models. A comprehensive summary of
409 previous model attempts, with their different settings and parameters, advantages and
410 shortcomings has been presented in Elsworth et al. (2014). In contrast, we set out to
411 compare different *conceptual* and *contrasting* models that explain the ongoing inflation of
412 Montserrat and the eruption potential in the near future, rather than adding another purely
413 elastic model to the collection. First, we considered and then excluded dykes and faults as a
414 tectonic component of deformation. Second, we introduced geometries with non-rotational
415 symmetry, and finally, we move in the following to visco-elastic models (Models V_H, VZ) and
416 focus on the distal stations only. We drop the shallow elliptical source in our considerations
417 as it only affects the closer stations (see Fig. 5), the deformation data of which might be
418 masked by loading effects (Odbert et al., 2015) rather than revealing deep source processes
419 we are interested in. We use in the following the depth-extended ellipsoidal geometry (same
420 as Model E_{1EX} and depicted in Fig. 6) with an initial volume of about 8 km³.

421 **5. A visco-elastic model for the Montserrat eruption**

422 In the previous sections we ruled out tectonic sources and dykes as sole deformation
423 sources and established a source geometry which, applied to volume or pressure changes
424 can explain the deformation data on Montserrat throughout the course of the eruption. The
425 choice of an elliptical geometry in contrast to an isotropic, rotational symmetry or a more

426 realistic, detailed crustal model is not vital compared to the fundamental question whether
427 the volcanic system of Soufrière Hills volcano is further pressurising by continued magma
428 influx or other pressurising mechanisms, or volcanic activity is finally declining, even at
429 depth. So far, the deformation pattern has been interpreted as a magma drainage and
430 extrusion for phases, and renewed magma influx or pressurisation for pauses; in the
431 following we test a hypothesis to re-interpret the inflation pattern during pauses in a
432 fundamentally different way.

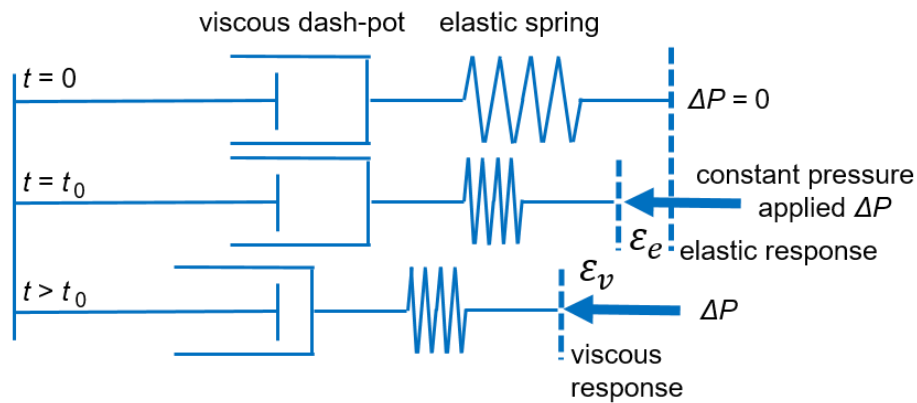
433 **5.1. Petrological indications for the end of a magma intrusion**

434 The recent study by McGee and co-authors (2019) has provided a strong suggestion that the
435 magma intrusion below SHV might have ended sometime in 2004 (from Phase 3 onwards),
436 based on a comparison of mafic enclaves and andesitic host rock over the entire period
437 between 1995 and 2010. They used the short-lived isotopes ^{210}Pb and ^{226}Ra in the Uranium
438 series decay chain as an indicator for volatile transfer and loss in both the enclaves and the
439 host andesite to reveal significant changes over time. While erupted andesite has been
440 almost entirely in equilibrium or has shown deficits of ^{210}Pb indicating continuous volatile loss
441 before and throughout the eruption, most of the mafic enclaves have shown an excess of
442 ^{210}Pb , interpreted as volatile enrichment that has lasted over a decade. The highest
443 $^{210}\text{Pb}/^{226}\text{Ra}$ ratios have been determined from enclaves in Phase 2, decreasing continuously
444 afterwards. This pattern has been explained by a cutting off fresh gas influx in the deeper
445 mafic system from Phase 3 onwards. The ^{210}Pb excess can be modelled by one single,
446 extended intrusion of basaltic magma at depth (carrying fresh gas), probably intruded in
447 1992 coinciding with the occurrence of deep seismicity. Hence, the intrusion might have
448 ended with Phase 2, when the gas influx decreased preventing further build-up of ^{210}Pb .

449 **5.2. Generalised Maxwell rheology**

450 Visco-elastic models have been employed by several studies (e.g. Del Negro et al., 2009;
451 Gottsmann and Odbert, 2014; Hickey et al., 2016), and a comprehensive overview on

452 rheological models can be found in Head et al. (2019). Based on the petrological
 453 considerations in the previous section we have contemplated an alternative explanation for
 454 the inflating deformation patterns during pauses as the ongoing response of a viscous crust
 455 to an initial intrusion from 1992 through 2003, excluding any additional magma influx
 456 afterwards. We use the ‘saw-tooth’ deformation pattern in the iconic MVO overview plot
 457 depicted in Fig. 2 and refer to the behaviour of the distal stations (MVO1 and NWBL) as they
 458 are most strongly indicative for the processes of the deeper magmatic system. Striking
 459 features that have guided our modelling attempts are the slightly declining steepness of
 460 inflation during pauses while the deflation phases show a steepening trend. Furthermore, we
 461 have recognised an almost perfect linear behaviour in both phases and pauses that
 462 suggests a visco-elastic behaviour represented by a Maxwell rheology illustrated in Fig. 9.



463
 464 *Figure 9: Three stages of visco-elastic response using Maxwell rheology; system in*
 465 *equilibrium at $t = 0$, pressure step ΔP at time t_0 , long-term response for $t > t_0$.*

466
 467 A Maxwell rheology is characterised by a viscous- and an elastic element in series where ϵ_e
 468 and ϵ_v are the elastic and viscous strain responses, respectively, at $t > t_0$ to a step-like
 469 pressure pulse ΔP at time $t = t_0$. The total strain response is given by adding these
 470 components

471
$$\epsilon_{\text{total}} = \epsilon_e + \epsilon_v, \quad (9)$$

472 or in terms of pressure

$$479 \quad \varepsilon_{\text{total}}(t) = \frac{\Delta P}{E} + \frac{\Delta P}{\eta} t, \quad (10)$$

473 where E is Young's modulus and η the viscosity. Depending on the dimension, direction and
474 the medium considered E can be replaced by rigidity (shear modulus) or incompressibility
475 (bulk modulus), and accordingly, η can be either shear or bulk viscosity. Eq. 10 implies an
476 immediate, time-independent elastic response, and a viscous response that is linear in time
477 and continuous as long as the pressure ΔP is applied. In our case the elastic parameter is
478 the shear modulus μ and η the shear viscosity.

480 The Generalised Maxwell model comprises several Maxwell branches and in addition a
481 parallel, purely elastic branch where the elasticity value is partitioned between all branches.
482 In its simplest form the generalised model consists of only one Maxwell- and one elastic
483 branch and is referred to as Standard Linear Solid (SLS) where elasticity is partitioned as μ_1
484 and μ_2 (Fig. 10). This results in strain patterns that react to pressure changes with a delayed
485 response, the characteristic time τ , which is dependent on the choice of viscosity and
486 elasticity partitioning. Hence, the linear time-dependent response of the Maxwell rheology is
487 replaced by

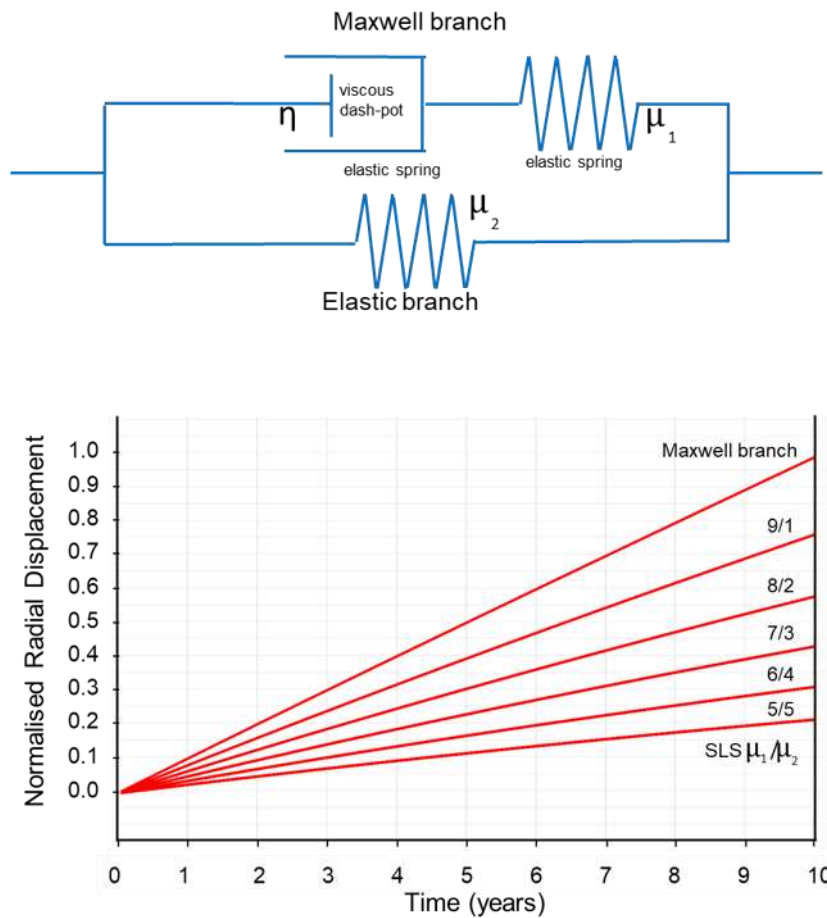
$$489 \quad \varepsilon_{\text{total}}(t) = \frac{\Delta P}{\mu_2} \left(1 - \frac{\mu_1}{\mu_1 + \mu_2} e^{-\frac{t}{\tau}} \right) \quad (11)$$

488 with the characteristic (retardation) time

$$495 \quad \tau = \eta \frac{\mu_1 + \mu_2}{\mu_1 \mu_2}. \quad (12)$$

490 While the partitioning of the elastic modulus between the two branches offers an additional
491 degree of freedom to fit observational data, the two elasticity values lose their original
492 physical meaning. Lin (2020) describes this split of elasticity into two branches by an
493 additional parameter $g = \mu_1/(\mu_1 + \mu_2)$, that varies between 0 and 1, governing the ratio of
494 viscous fluids to solids in a visco-elastic solid, e.g. partial melt to solid rock. As a

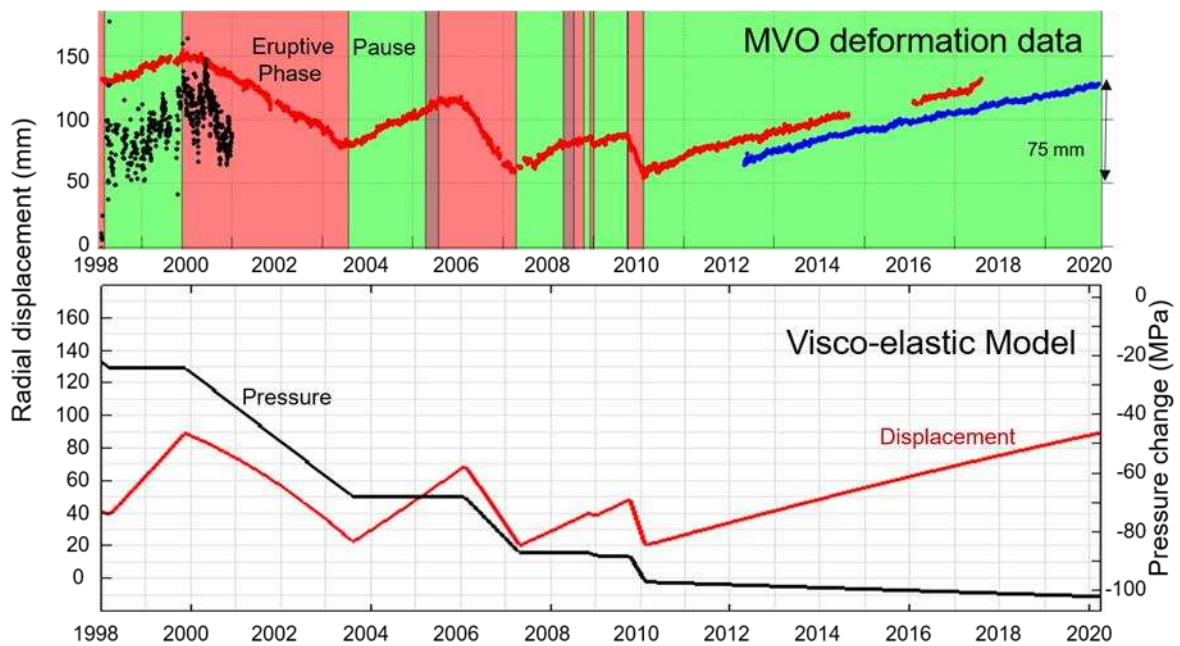
496 consequence, the choice of μ_1 and μ_2 might be depth/temperature-dependent but is often
 497 kept constant as $\mu_1 = \mu_2 = 0.5 \mu$ (e.g. Del Negro et al., 2009; Head et al., 2019).



498
 499 *Figure 10: Comparison between Maxwell rheology and SLS with varying elasticity*
 500 *partitioning μ_1 and μ_2 . While the pure Maxwell branch has a linear time dependence here*
 501 *depicted for 10 years (see Eq. 10), the SLS reduces the amplitude and shows a curved*
 502 *trajectory due to the retardation time τ and parameters within (see Eq. 11 and 12). This*
 503 *example is based on Young's modulus $E = 10 \text{ GPa}$, pressure step $dP = 20 \text{ MPa}$, and*
 504 *viscosity $\eta = 10^{19} \text{ Pas}$.*

505
 506 Fig. 10 shows the impact of the choice of μ_1 and μ_2 in comparison with the Maxwell rheology;
 507 progressive partitioning between μ_1 and μ_2 results in reduced amplitudes of deformation, for
 508 high viscosities the SLS converges to a purely elastic system. A higher pressure is

509 necessary in an SLS (compared to a Maxwell rheology) to explain the same deformation.
 510 Hence, Maxwell- and a purely elastic model are endmembers bracketing the range of
 511 pressures to explain the amplitude of a deformation pattern. By considering these
 512 endmembers in realistic visco-elastic parameter distributions we have attempted to gain
 513 insight into upper and lower bounds of magma influx or pressurisation.
 514 Given the intriguingly linear behaviour and the abrupt changes between pauses and phases
 515 in the deformation pattern, we start to explore the parameter space with a pure Maxwell
 516 rheology (Fig. 9) in a simplified model with homogeneous viscosity η and Young's modulus
 517 E , describing the visco-elastic crust surrounding the magma (Model V_h). In this case the
 518 linear behaviour during pauses is only dependent on shear viscosity and the residual
 519 reservoir



520

521 *Figure 11: Comparison of the radial deformation at station MVO1 (upper panel, from Fig. 2)*
 522 *with the modelling results (lower panel) for the same station as a visco-elastic response*
 523 *using a Maxwell rheology (Model V_h). Results are shown for a constant Young's modulus of*
 524 *10 GPa, a constant viscosity of 3.3×10^{18} Pas, and a depressurisation and reservoir volume*
 525 *change equivalent to 100 MPa. Note that in this model a slight change in the deformation*
 526 *gradient in Pause 5 is achieved by a small pressure decrease during the pause.*

527 pressure once magma extrusion has stopped while phases are also governed by shear
528 modulus and the decreasing pressure caused by volume loss during the phases. The model
529 setup comprises the vertically extended ellipsoid of Fig. 6 (same as Model E_{1EX}) embedded
530 in a homogeneous half space. Following this approach we have derived a set of
531 homogeneous models that equally match the deformation pattern (see Fig. 11) using
532 viscosities in the range of $\eta = [1.8 \times 10^{18}, 1.2 \times 10^{19}]$ Pas and a Young's modulus ranging $E =$
533 $[5, 10]$ GPa.

534 According to Eq. 10, the linear trend we have seen in Pause 5 which we have attempted to
535 interpret as a visco-elastic response to an initial magma intrusion rather than as a continued,
536 buoyant magma influx, is only dependent on constant pressure and the viscosity, which in
537 turn is controlled by the crustal temperature distribution. To keep the residual pressure
538 constant during a pause we have assumed the modelled magma intrusion to be connected
539 to a larger, deeper reservoir such that the small volume change due to inflation can be
540 compensated by mass transfer from the reservoir. Magma compressibility plays an
541 additional role in pressure recovery and inflation as discussed by Segall (2016).

542 In the following we explore the wide range of depth-dependent temperature and resulting
543 viscosities and their influence on the deformation models.

544 **5.3. Temperature and viscosity dependence**

545 The exact temperature distribution on Montserrat is controlled by several factors such as
546 hydrothermal activity and the accurate location and history of the magma intrusion, which is
547 subject to large uncertainties. These large uncertainties are also reflected in the literature:
548 Manga et al. (2012) measured temperature gradients near the seafloor in the Lesser Antilles
549 and found values between 0.06 K/m, and up to 0.1 K/m in a borehole at the arc crest
550 between Montserrat and Guadeloupe at a water depth of 1200 m and borehole depth of 280
551 m. Geothermal investigations on Montserrat found temperatures of 200 °C (473 K) at 2000
552 m depth over a wide area surrounding the volcanic centre (Ryan & Shalev, 2014) leading to

553 a shallow temperature gradient of 0.1 K/m. Gottsmann and Odbert (2014) implemented in
554 their models an island-wide crustal hot zone of 1373 K between 31 km and 27 km depth
555 superimposed to an elevated crustal heat flow modelled by one or two crustal magma
556 reservoirs. Similar to Gottsmann and Odbert (2014), we have implemented a thermal model,
557 based on the source geometry we found in Section 4 for the intrusion, which is underpinned
558 by a deeper magma reservoir between 14 and 20 km depth (e.g. Zellmer et al., 2003). This
559 deeper reservoir does not have any impact on the surface deformation which is controlled by
560 the deep-rooted intrusion modelled by the extended ellipsoid above. We use a temperature
561 of 900 K at 20 km depth, and 1350 K in the deep reservoir and intrusion. This corresponds to
562 thermal gradients of 0.075 K/m above the deep reservoir and 0.03 K/m further away from
563 reservoir and intrusion.

564 The Arrhenius approximation has been widely used to estimate shear viscosity $\eta(T)$
565 distributions from depth-dependent temperature models (e.g., from basaltic magmas, Del
566 Negro et al., 2009; to silicic compositions, Le Mével et al., 2016)

$$579 \quad \eta = A e^{\left(\frac{H}{RT}\right)}, \quad (13)$$

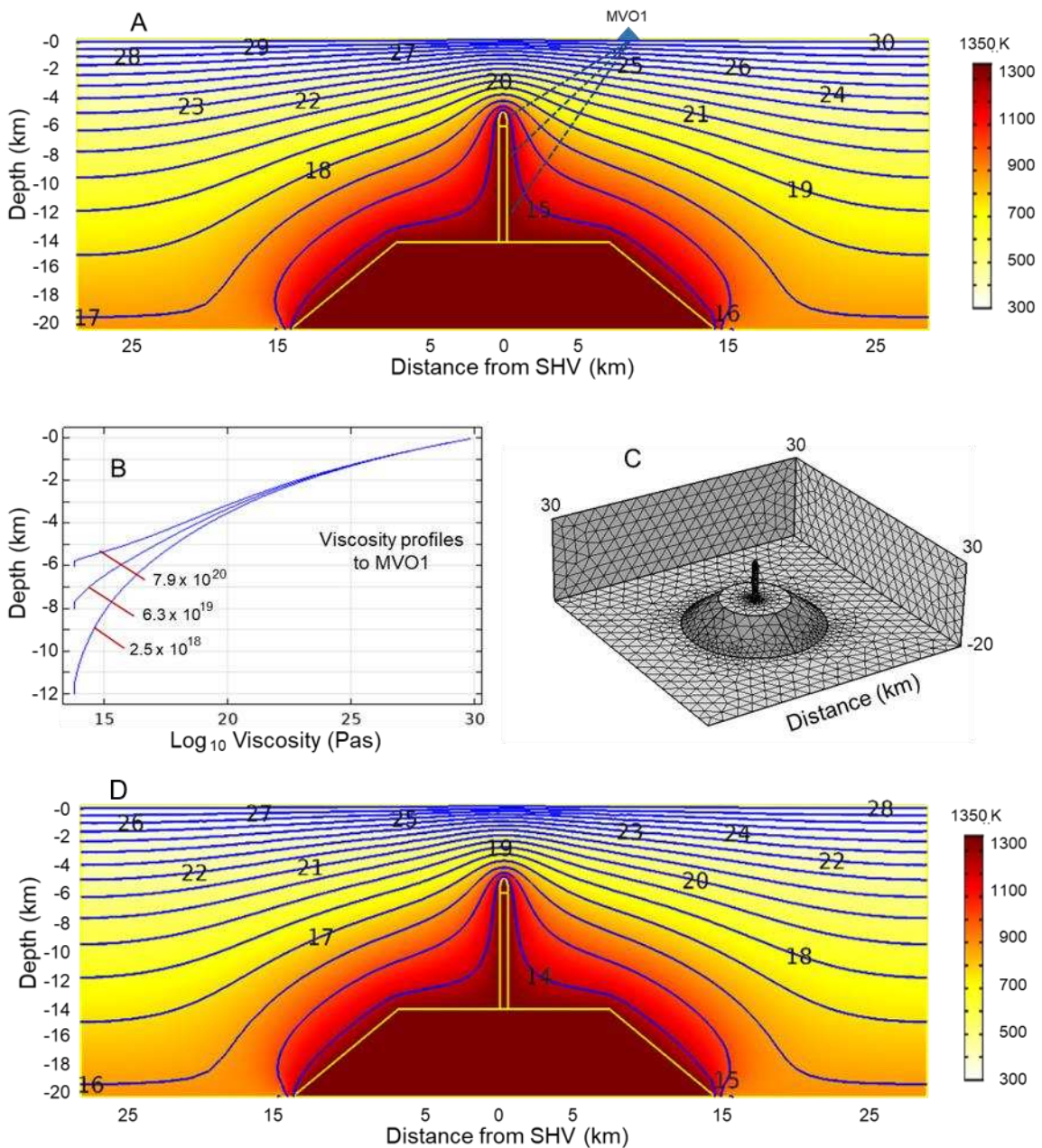
567 where A is the Dorn parameter, H is the activation energy, R is the ideal gas constant, and T
568 is temperature in degrees K. Recent visco-elastic studies have employed commonly used
569 values for A and H that are potentially representative of the geochemical composition and
570 subsurface temperature. In contrast, Morales Rivera et al. (2019) have explored the full
571 range of these parameters by applying thermo-mechanical models to the 2010-2011 unrest
572 of Taal volcano, Philippines, investigating how host rocks with distinct viscosity endmembers
573 in the Arrhenius formulation affect the response of the Earth's surface due to magma
574 reservoir pressurization. In their study they used a range of activation energies H between
575 106 kJ/mol to 217 kJ/mol, respectively, equivalent to a silicic and intermediate crust. Using
576 Eq. 13 leads to a range of viscosities spanning several orders of magnitude for the same
577 crustal temperature of 600 K. In the same study the Dorn parameter A is varied between $5 \times$
578 10^9 and 2×10^{13} Pas, again for a silicic and intermediate crust, adding another 4 orders of

580 magnitude difference for the same temperature. These examples demonstrate how large the
581 uncertainties in both temperature, and consequently in viscosity are.

582 For the next modelling step we have chosen values for the Dorn parameter $A = 10$ GPa \cdot s,
583 and the activation energy $H = 120$ kJ/mol previously used for Montserrat (e.g. Odbert et al.,
584 2015) and derive the viscosity distribution depicted in Fig. 12A. We have estimated a range
585 of potential temperature and corresponding viscosity values by profiling the area that
586 contributes most to the deformation field below the station MVO1. These profiles and the
587 resulting average viscosity values are depicted in Fig. 12B for the distal station MVO1. All
588 profiles converge towards the surface to viscosity values far above the range we employed
589 in our simplified homogeneous model. Therefore, we have tested the endmember models by
590 Morales Rivera et al., (2019) in the Arrhenius formulation Eq. 13 to find the lowest value
591 possible for a corresponding endmember in viscosity. This viscosity distribution (Fig. 12D) is
592 then used to compute the deformation pattern as a response to an initial intrusion without
593 any further pressurisation or magma influx. We refer to this viscosity distribution and Young's
594 modulus profile derived from Paulatto et al. (2019) and reduced to 67% and 11%
595 (Gudmundsson, 1990) as explained in Section 3, as the 'depth-dependent model', VZ_{Max} and
596 VZ_{SLS} , hereafter.

597 **5.4. Visco-elastic response to magma intrusion**

598 Using the Maxwell rheology introduced in Section 5.2 and the viscosity distribution derived in
599 Section 5.3 we can now model the visco-elastic response to an initial intrusion that is
600 followed by a stepwise depressurisation of a magma reservoir due to extrusion of magma
601 during Phase 2 through Phase 5, using the same pressure steps as employed in the
602 homogeneous model V_H (Fig. 11). We present in Fig. 13 the corresponding radial
603 deformation for GPS station MVO1 for a pure Maxwell rheology (VZ_{Max}), several SLS
604 rheologies (VZ_{SLS}) and a purely elastic model for reference (E_{1Ex}). In contrast to the

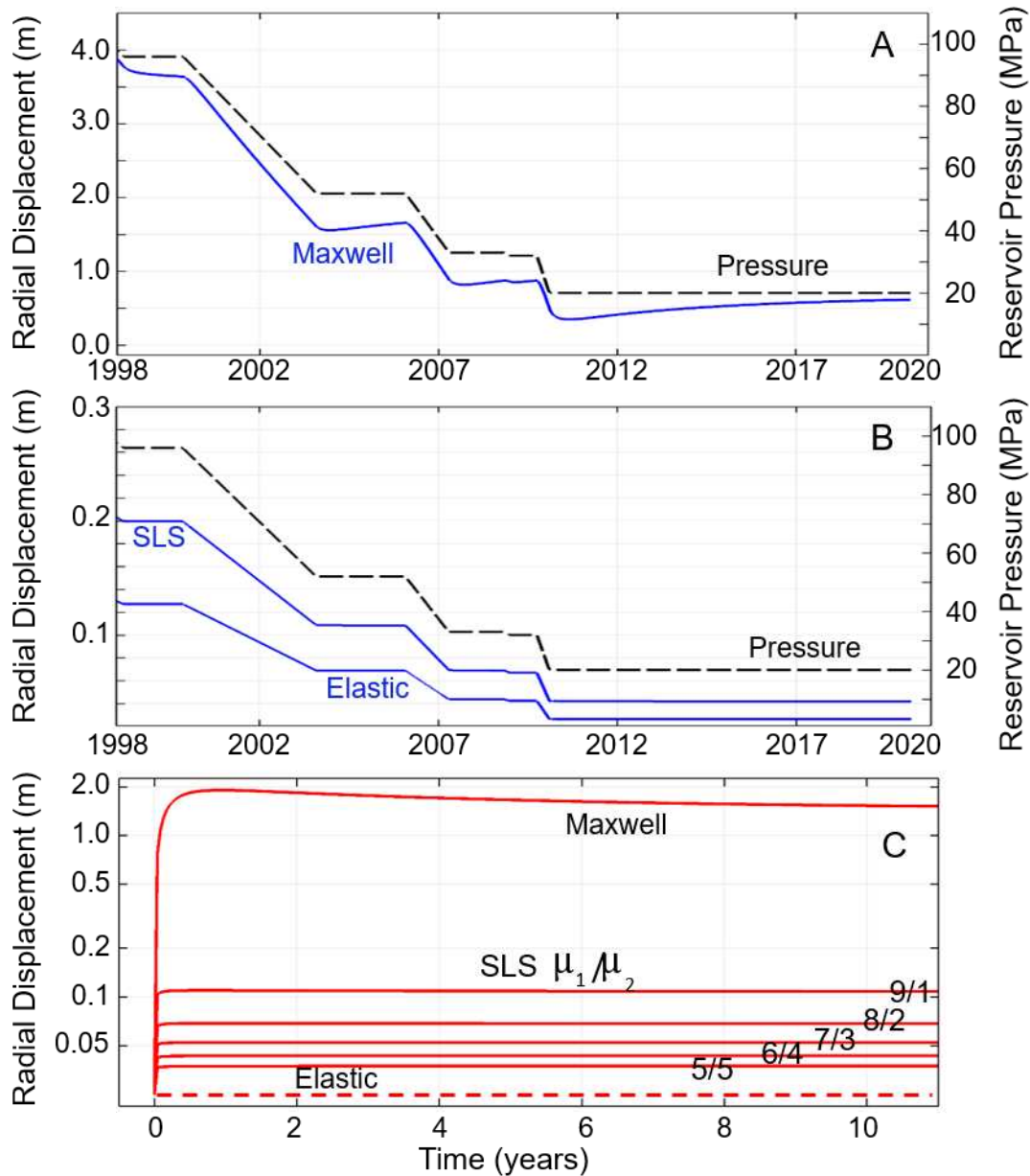


605

606 *Figure 12: Temperature – viscosity model VZ_{Max} . A: temperature distribution and contoured*
 607 *viscosity values (Log_{10}). Dashed lines indicate where viscosity profiles have been calculated*
 608 *between the magmatic source at different depths and distal GPS station MVO1. B: Viscosity*
 609 *profiles between MVO1 and magmatic source at 12, 8 and 6 km depth. Viscosity averages*
 610 *over the profiles are indicated. C: Meshed temperature model comprising cone shaped deep*
 611 *reservoir (30 km wide and 6 km high) and superimposed magma intrusion as depicted in Fig.*
 612 *6 left. D: endmember model for lowest possible viscosities which differ from (A) by one to*
 613 *two orders of magnitude.*

614 homogeneous model V_H in Fig.11 the deformation during the pauses when the pressure
615 stays constant does show a small inflationary trend for the Maxwell rheology (Fig. 13A)
616 which is in the same order of magnitude as the observation. However, this inflationary trend
617 is much smaller than the deflation during magma extrusion resulting in an overall deflation
618 which follows the pressure profile over time, unlike the observed saw-tooth pattern in Fig. 2
619 and 11. In fact, the small inflationary trend is well explained by the dissipation of crustal
620 stress exerted by the initial intrusion. The more realistic depth-dependent model reveals the
621 interaction between regions of different properties. Here elastic energy is stored in layers
622 with high viscosity after the initial pressurisation and then dissipated due to the viscous
623 behaviour of regions with lower viscosity. This behaviour has been previously noted and
624 modelled by other studies (e.g. Yamasaki et al., 2017) and is demonstrated in Fig. 13C
625 depicting the crustal response to a positive pressure step of 20 MPa for Maxwell and SLS
626 rheology over 10 years. Here the homogeneous visco-elastic model V_H (Fig. 11) is replaced
627 by the same depth-dependent, visco-elastic model used VZ_{Max} for Fig.13A. Unsurprisingly,
628 the SLS rheology (VZ_{SLS}) follows closely the pressure profile and the purely elastic behaviour
629 without any inflation trend during pauses (Fig. 13B).

630 We started from a simplified homogeneous model V_H (Fig. 11) where we determined a
631 viscosity-elasticity combination that could explain the 'saw-tooth' pattern observed in Fig. 2.
632 Despite using endmember viscosity profiles as close as possible to the low viscosities of the
633 homogeneous model, the 'saw-tooth' pattern cannot be reproduced by pauses during which
634 the pressure remains constant. Hence, we have to reject the hypothesis that the inflations
635 during pauses, particularly the ongoing inflation that has continued for more than 10 years,
636 can be explained by a delayed crustal response to an initial intrusion without any further
637 magma influx or pressurisation.



638

639 *Figure 13. A: Pattern of radial deformation at MVO1 for depth-dependent visco-elastic model*
 640 *derived in Section 5.3 and Maxwell rheology (VZ_{Max}) using the same depressurisation steps*
 641 *as in the homogeneous model (V_H) in 5.2. B: same for SLS rheology. C: Response of depth-*
 642 *dependent model used in A to a positive pressure step of 20 MPa for different rheology*
 643 *models. Note the logarithmic amplitude scale.*

644

Parameter	Description	
V_{Source}	Source Volume	m^3 (calculated)
V_{DRE}	Volume of erupted material (DRE)	m^3 (Wadge et al., 2010)
ρ_{DRE}	Density of erupted material (DRE)	2600 kg/m^3
ρ_{M}	Density of magma	kg/m^3 (calculated)
β_{M}	Compressibility of magma	Pa^{-1} (calculated)
E	Young's Modulus	1.3 – 12.2 GPa (Paulatto et al., 2019; reduced to 11% - 67%)
ν	Poisson Ratio	0.25
η	Viscosity	Pas (calculated)
β_{s}	Compressibility of source reservoir	Pa^{-1} (calculated) (Huppert & Woods, 2002)
β_{r}	Rock bulk modulus	$E/3(1-2\nu)$
n	Exsolved gas content	wt.% (calculated)
N	Total gas content	4 – 8 wt.%
ρ_{g}	Gas density	kg/m^3 (calculated)
ρ_{c}	Crystal density	2600 kg/m^3
ρ_{m}	Melt density	2300 kg/m^3
x	Crystal content	40 %
M	Molecular mass of water	0.01801528 kg/mol
P	Pressure	Pa (calculated)
R	Universal Gas content	8.314 J/mol K
T	Temperature	300 - 1350 K
dT/dz	Thermal Gradient	0.03 – 0.1 K/m
A	Dorn Parameter	$5 \times 10^9 - 10^{10} \text{ Pas}$
H	Activation Energy	$1.06 \times 10^5 - 2.17 \times 10^5 \text{ J/mol}$

645

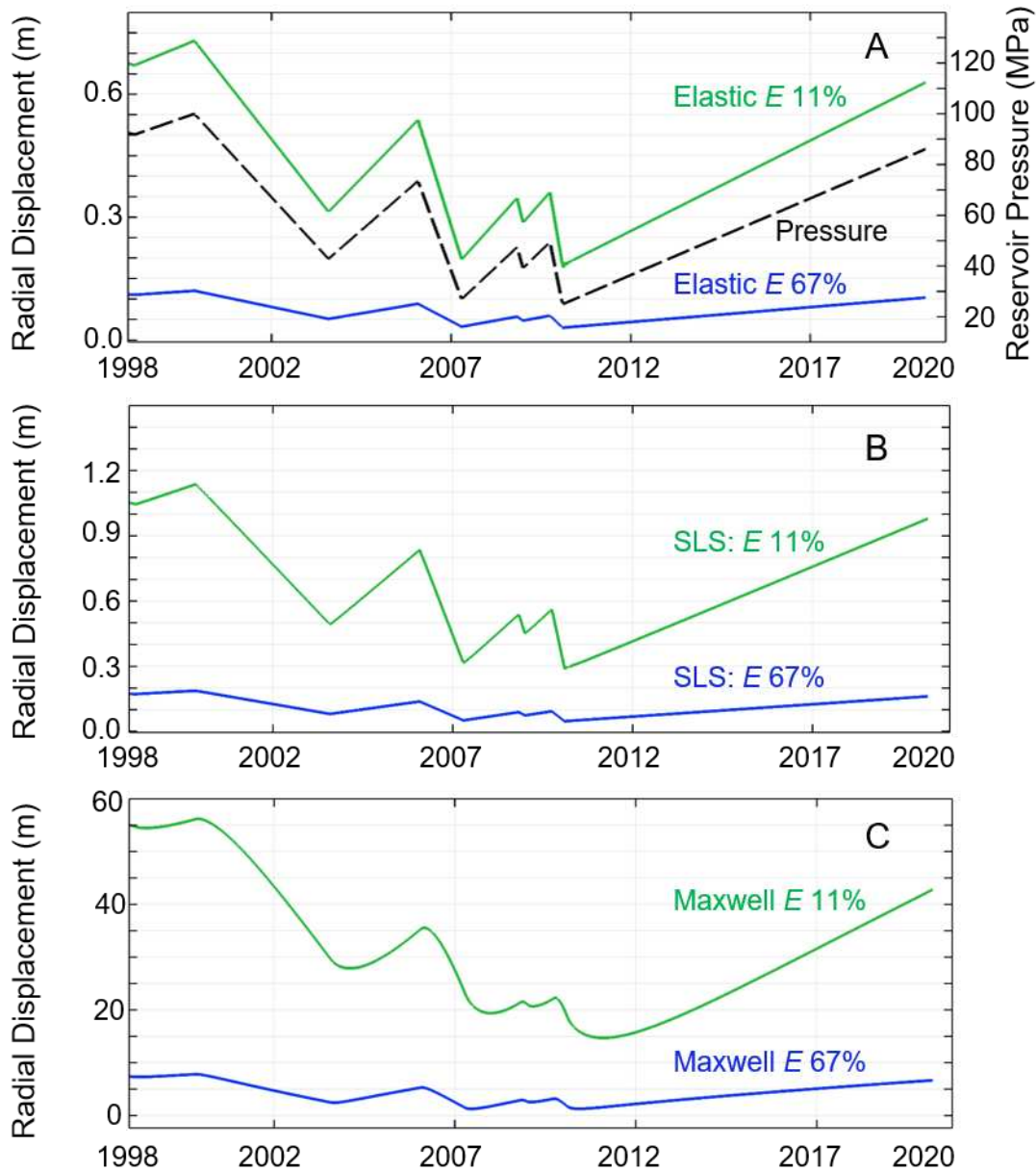
646 *Table 2. Variables used in the compressibility calculations and deformation models.*

647 **6. Discussion**

648 Based on the elastic models of Section 4 we have re-introduced pressurisation during
649 pauses in the following set of numerical models, and have estimated to what extent such
650 pressurisation can be reduced by visco-elastic rheologies developed in the previous section.

651 Using purely elastic behaviour, SLS and the Maxwell rheology we have attempted to find
652 endmembers of pressurisation values, for which we discuss potential physical processes
653 that explain the observations in Pause 5.

654



655

656 *Figure 14: Radial displacement at station MVO1 for indicated rheology and Young's*
 657 *modulus. E 11% and E 67% refer to the revised seismic velocity depth profile of Paulatto et*
 658 *al. (2019) reduced to 11% and 67%, respectively, as explained in Section 3. In all cases the*
 659 *same pressure history has been applied. A: purely elastic cases, B: SLS with equally shared*
 660 *shear modulus $\mu_1 = \mu_2$, C: Maxwell rheology. Note the different scales in A, B and C.*

661 6.1 Final numerical deformation models

662 The modelling results displayed in Fig. 14 have been obtained by applying the same
 663 pressure values and history as depicted in panel A, hence, resulting in different radial

664 displacements according to the choice of rheological model. By scaling these radial
665 displacements to the observations throughout the eruptive history we have determined the
666 time line and values for pressurisation and depressurisation that correspond to the
667 observations. We drop the extreme case in panel C (Fig. 14) for a Maxwell rheology
668 combined with an elasticity value reduced to 11% as the overall temporal pattern does not fit
669 the observations. All pressure differences throughout the eruption are listed in Table 3.
670 Focussing on Pause 5 we obtain pressurisations dP/dt ranging from 0.1 MPa/year to 6
671 MPa/year for Maxwell (VZ_{Max}) and purely elastic case (E_{1Ex}), respectively.

Phase/Pause	Estimated DRE (10^6 m^3) (Wadge et al, 2014)	Pressure change (MPa) Elastic models E reduced to		Pressure change (MPa) SLS models E reduced to		Pressure change (MPa) Maxwell model E reduced to 67%
		11%	67%	11%	67%	
1	331	-1	-8	-1	-5	-0.1
1		1	8	1	5	0.1
2	336	-9	-57	-7	-37	-0.7
2		5	30	4	20	0.3
3	282	-8	-46	-5	-30	-0.6
3		4	20	2	13	0.3
4	39	-2	-8	-1	-5	-0.1
4		2	10	1	7	0.1
5	74	-4	-24	-2	-16	-0.3
5		10	61	6	39	0.8
dP/dt		1	6	1	4	0.1
dV/dt [m^3/year]		3.5×10^6		4.2×10^6		18×10^6
dV/dt [m^3/s]		0.11		0.13		0.57

672

673 *Table 3. Pressure changes for different models that explain the deformation patterns at*
674 *MVO1 for all phases and pauses. The last three rows show the corresponding pressurisation*
675 *rates and volumetric strain changes during Pause 5.*

676 The corresponding volume changes are determined by the volumetric strain integral over the
677 intrusion (geometry Fig. 7) during inflation and result in $0.11 \text{ m}^3/\text{s}$ to $0.57 \text{ m}^3/\text{s}$ or 3.5×10^6
678 m^3/year to $18 \times 10^6 \text{ m}^3/\text{year}$ for the elastic and Maxwell case, respectively. As expected, the
679 corresponding values for the SLS rheology are closer to the elastic case (Table 3).

680

681 **6.2 Mass balance for compressible magmas**

682 According to Wadge et al. (2014), Phase 3 involved the extrusion of $282 \times 10^6 \text{ m}^3$ DRE
 683 (Table 3). This is a factor of about 10 times larger than the volume change derived for an
 684 elastic model E_{1Ex} and twice the volume for a visco-elastic Maxwell model VZ_{Max} . However,
 685 this can be accounted for by the effect of magma compressibility at reservoir pressures.
 686 Using Equations (6) through (8) in Section 4.6 we estimate the equivalent, depth dependent
 687 volume changes for compressible magma with a 40% crystallinity and volatile content of 4 –
 688 6 wt.%; in Fig. 15 results for Phase 3 and Phase 5 are compared.

689

Phase/Pause	Estimated DRE (10^6 m^3)	Volume change (10^6 m^3) Elastic model	Volume change (10^6 m^3)	
			SLS	Maxwell
1	331	-5	-5	-13
1		5	5	22
2	336	-33	-39	-190
2		18	20	69
3	282	-27	-31	-122
3		12	13	25
4	39	-5	-5	-8
4		6	7	15
5	74	-13	-15	-29
(10 years) 5		35	42	180

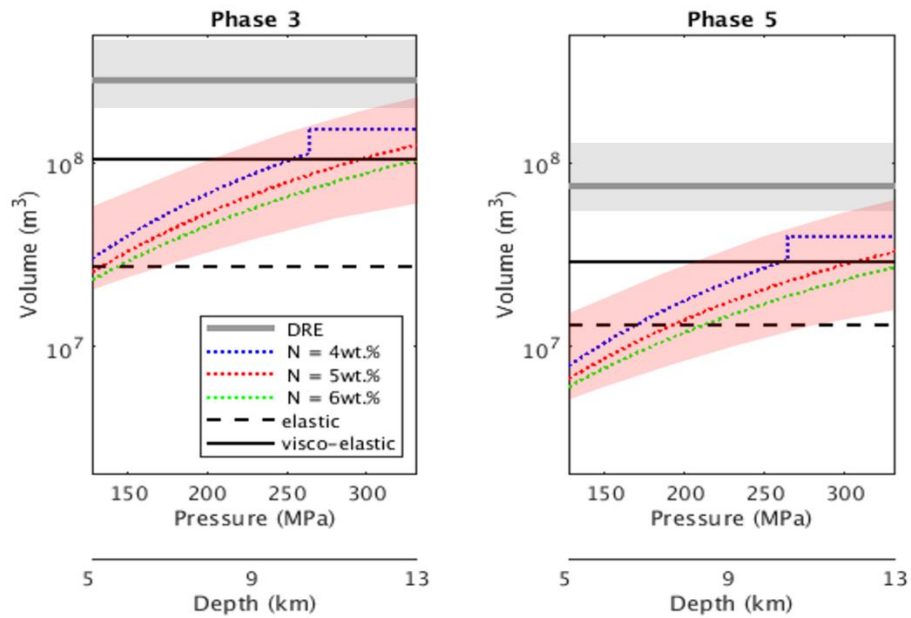
690

691 *Table 4. Deep source volume change from our elastic (E_{1Ex}) and visco-elastic models (VZ_{Max}
 692 and VZ_{SLS}) compared to estimated DRE volumes ($\pm 50\%$) from Wadge et al. (2014). Model
 693 parameters correspond to those used in Fig. 14.*

694

695 The modelled volumes for Maxwell and the elastic case are the output of the volumetric
 696 strain integral over the entire depth range displayed as horizontal lines while the DRE
 697 equivalent volumes corrected for compressibility due to 4 – 6 wt.% H_2O content are given as
 698 depth-dependent. This shows that four times more material was erupted during Phase 3
 699 compared to Phase 5. The elastic model underestimates the volume change at reservoir

700 level for Phase 3 while the visco-elastic model appears to slightly overestimate the volume
 701 change at reservoir level for Phase 5. This could point to a decrease of volatile content in the
 702 remaining magma during the years between 2006 (Phase 3) and 2010 (Phase 5) causing a



703

704 *Figure 15: Comparison between the estimated DRE volume and the modelled source*
 705 *volume change during Phases 3 and 5 for an elastic model (dashed black line) and a visco-*
 706 *elastic Maxwell model (solid black line). These volume changes are based on the modelled*
 707 *GPS data listed in Table 2 integrated over the depth range between 5 and 13 km. Dotted*
 708 *lines are corresponding, depth-dependent volumes corrected for magma compressibility for*
 709 *different initial gas contents (4 - 6 wt.%) and a crystallinity of 40%. Note the step for 4 wt.%*
 710 *due to the solubility limit at about 260 MPa. Uncertainty on DRE (grey) and corresponding*
 711 *compressible magma volume (pink) are based on the DRE estimation of ±50% (Wadge et*
 712 *al., 2014). The depth scale indicated assumes lithostatic pressure with a rock density of*
 713 *2600 kg/m³.*

714 decrease in compressibility. Alternatively, this could also be interpreted as a continued influx
 715 of magma during extrusion for Phase 5. However, both elastic and visco-elastic models
 716 match in general the estimated DRE volumes once compressibility is taken into account and

717 suggest that the models brace the realistic set of parameters that explain the deformation
718 pattern throughout the eruption.

719 The apparent volume changes obtained through our numerical models need to be translated
720 into DRE volumes according to eq. 6 in section 4.6 to reflect the actual mass of magma
721 intruded into the reservoir. The factors $\rho_{\text{DRE}}/\rho_{\text{m}}$ and $(1 + \beta_{\text{m}}/\beta_{\text{c}})^{-1}$ in Eq. 6 represent the effects
722 of compressibility of magma and reservoir, respectively. Hence, using the volumes for Phase
723 5 in Table 3 and the apparent volume change rates in Table 2, we obtain correction factors
724 of 5.7 and 2.6 for the elastic and Maxwell case, respectively. Applying those to the apparent
725 volume change rates we finally obtain 0.62 m³/s to 1.48 m³/s or 19 x 10⁶ m³/year to 47 x 10⁶
726 m³/year for the elastic and Maxwell cases, respectively.

727 **6.3 Link to SO₂ outgassing**

728 Focussing on Pause 5 and the ongoing inflation of the island of Montserrat, another way to
729 constrain the assumption of continuing magma influx as an explanation is a comparison with
730 the outgassing of SO₂. Both traverse-based and network data acquisition place the amount
731 of outgassed SO₂ in the range of 300 ± 130 tonnes/day (Stinton et al., 2020).

732 Crystallisation during cooling (second boiling) reduces the volume of melt and, therefore,
733 increases the vapour pressure forcing volatiles to exsolve and form bubbles. Even a partial
734 confinement of these exsolved volatiles results in pressurisation of the magma reservoir, and
735 hence, will contribute to the deformation field. If we assumed crystallisation as the sole
736 mechanism to explain the deformation data and made the rather extreme assumption of a
737 closed system where no exsolved gas can escape, a source volume of 40 km³ would be
738 required (Caricchi & Simpson, 2015) to generate the amount of gas needed matching a
739 pressurisation of 1 – 6 MPa/year. While this volume is in agreement with the magma volume
740 suggested by Christopher et al. (2015), it is significantly larger than our modelled sources
741 ranging from 1.26 km³ to 8 km³, and the amount of volume generated by a uniformly
742 degassing magma body of 40 km³ would have to be concentrated in the upper part of our

743 modelled intrusion in order to match the observed deformation data. Furthermore, the
744 assumption of a sealed system seems unrealistic given the constant outgassing of SO₂ at
745 300 tonnes/day during Pause 5, and we conclude that crystallisation induced degassing can
746 only account for a very small fraction of the observed deformation data.

747 If we assume an open system and hypothesise that the entire amount of sulphur originates
748 from a continuous influx of more mafic magma into a shallow intrusion we can obtain an
749 upper bound of magma influx that is constrained by the long-term average of SO₂ output.
750 Edmonds et al. (2014) estimated the amount of sulphur gases emitted continuously between
751 July 1995 and July 2011 at $4.0 \pm 0.6 \times 10^9$ kg while the total amount of magma erupted in 5
752 phases during this time amounted to 1.1 km³ (Wadge et al., 2010). Having found very little
753 sulphur (<100 ppm) in melt inclusions, Edmonds et al. (2014) assumed that all of the sulphur
754 emitted continuously over these years had resided as a volatile phase in the andesitic
755 magma reservoir prior to the onset of eruption. Adopting the numbers by Edmonds et al.
756 (2014) above, and assuming a magma density of 2600 kg/m³, we estimate the sulphur
757 content at about 0.14 wt%. Using the postulated volume influx in the range $dV/dt = [0.62,$
758 $1.48]$ m³/s, this results in a magma mass influx of $dM/dt = [139, 332] \times 10^6$ kg/day, of which
759 sulphur contributes 0.14 wt%. Hence we derive $[195, 465] \times 10^3$ kg/day of sulphur or about
760 $[390, 930]$ t/day of emitted SO₂ based on our purely elastic model or the visco-elastic
761 Maxwell model, respectively. These results are higher but overlap with the uncertainties of
762 the measured outgassing of 300 ± 130 tonnes/day and indicate that values of 1.48 m³/s or
763 47×10^6 m³/year form indeed an upper bound of magma influx into the deep reservoir.

764 **7. Summary and conclusions**

765 We embarked on an attempt to explain the current deformation pattern on Montserrat
766 showing since 2010 a continuous expansion of the entire island, which has important
767 implications in terms of understanding the future eruption potential of the volcano. We made
768 use of the remarkable similarity of deformation patterns that can be applied to both inflation
769 and deflation, hence one source geometry can be used for the entire eruptive history.

770 Through numerical modelling we have matched GPS data sets to a deep source embedded
771 in an elastic half space. Unlike other studies it has not been our intention to match all details
772 of the deformation data which can be achieved by varying parameters like viscosity,
773 elasticity, temperature in three dimensions. In contrast, we have explored alternative models
774 as proof of concept. Prompted by the petrology study of McGee et al. (2019) that suggested
775 the end of an initial magma intrusion by 2003, we have explored a set of visco-elastic
776 models, testing whether the entire deformation pattern throughout the eruptive history can be
777 explained by a visco-elastic response of the volcanic system to an initial intrusion without
778 any further pressurisation during eruptive pauses. Rather than searching for one possible
779 explanation, we attempted throughout this study to capture the widest possible range of
780 modelling parameters in order to assess the range of possible solutions that could explain
781 the deformation pattern on Montserrat.

- 782 • In our initial modelling attempts (Model I_S, I_D and I_F) we ruled out a dyke or fault to
783 explain the deformation on Montserrat. Given the fact that there is little evidence for
784 significant recent activity on the local faults as discussed in Section 4.2, we adopt a
785 more realistic tectonic contribution of max. 3 mm/year in each direction (Wadge et al.,
786 2014) which would correspond to a pressure reduction by only 1 MPa at the deep
787 source geometry. Hence, we conclude that any tectonic contribution to the current
788 deformation field has by comparison a very small impact.
- 789 • We conclude that the ongoing deformation pattern (Pause 5) is best explained using
790 a dual-source model (Model E_{2E}/E_{2Ex}) with a shallow deflating source and a deeper
791 inflating source. In terms of understanding the future eruption potential of the
792 volcano, continuous magma accumulation is the main consideration, therefore, it is
793 the deeper, inflating source which is more important. However, the deflating source
794 suggests a depressurisation at shallow depths. The observation that the shallow
795 source is not evident in the GPS data for any other phase or pause, other than Pause
796 5, implies it represents either a change in source process, or an ongoing process, the

797 effects of which were previously masked by the deeper source. Potential causes for
798 the deformation pattern close to the volcano and modelled as a shallow deflating
799 source could include cooling, crystallisation, outgassing and deposit loading. The
800 most viable explanation for deep source volume changes is magma accumulation,
801 whereas local and regional tectonics as well as crystallisation play a minor role, if any
802 at all.

- 803 • We have tested the hypothesis that the inflation during pauses could be due the
804 visco-elastic response of the volcanic system under constant pressure but without
805 further magma influx. By utilising the linear deformation trend of a Maxwell rheology
806 we found a set of parameters that could indeed explain the saw-tooth pattern for a
807 simplified, homogeneous model (V_H). For more realistic, depth-dependent parameter
808 distributions (V_Z), however, we reject the hypothesis explaining the saw-tooth pattern
809 without new magma influx. This is the case for all visco-elastic models we used
810 despite stretching the parameter space concerning temperature and viscosity as far
811 as possible.
- 812 • Our modelling has shown that the deformation data captured by the GPS network are
813 controlled by the upper surface of the source volume and extending the source
814 vertically, whilst maintaining its footprint, does not significantly alter the horizontal or
815 vertical displacements. Hence, the absolute volume of the magma body to which
816 volume changes are applied is hard to constrain and our preferred source geometry
817 is not incompatible with previously published source volumes (summarised in
818 Elsworth et al., 2014).
- 819 • By assuming a consistent source mechanism and geometry throughout the eruption,
820 we have mapped the deformation field for all phases and pauses into volume
821 changes at the deeper source, and conclusions can be drawn about magma supply
822 and extrusion rates. We have calibrated our best-fit model parameters in Pause 5
823 and have applied those to the GPS data in previous phases and pauses. By retracing

824 the entire eruptive history of SHV we have derived the total volume changes at the
825 deep source level. Fig. 8 summarises and compares the volume of erupted material
826 (DRE) and volume changes at depth based on the initial elastic models E_{1E} , while
827 Table 3 contains the corresponding values derived from the volumetric strain integral
828 for the depth-dependent, more realistic set of elastic and visco-elastic models VZ.

- 829 • Regarding the timing of the start of Phases 2 – 5, it is significant that the volume
830 extruded has exceeded the volume of influx in each eruptive phase. This indicates
831 that the magma reservoir has not been replenished to its original pre-eruption volume
832 prior to the onset of the next eruptive phase. This fact demonstrates that the
833 sequence of eruptive phases is not merely controlled by the accumulation of a critical
834 magma volume, but another change in the system is required instigating an eruptive
835 phase. Following this apparent trend of onsets indicated in Fig. 8 an intriguing
836 interpretation could be made: the so-called ash-venting in the beginning of 2012
837 could be interpreted as a failed new eruptive phase.
- 838 • Another outcome of this study is the appreciation of how large the uncertainties in
839 modelling parameters are, preventing the modelling results to be further constrained.
840 This has been demonstrated in Elsworth et al. (2014) for purely elastic models and
841 for visco-elastic models by Morales Rivera et al. (2019), as well as this study.
842 Additional data sets like gravity measurements are needed to constrain the mass
843 influx more directly.
- 844 • Currently there are three criteria which are used to define the end of the eruption at
845 the Soufrière Hills volcano (Wadge and Aspinall, 2014). These are (i) absence of low
846 frequency seismic swarms, (ii) daily SO_2 fluxes below 50 tonnes/day, and (iii) no
847 significant volcanic ground deformation from a deep source. Currently the latter two
848 criteria are not being met. These two criteria are a proxy for continued input into the
849 crustal magma storage system from depth of a hotter, volatile rich, more mafic
850 magma. This input is thought to be necessary to sustain a long-lived, episodic

851 eruption such as observed at the Soufrière Hills volcano. An exploration of the effects
852 of a range of viscoelastic and elastic magma plumbing system models suggests that
853 the observed ground deformation is best described by a continued pressurisation of a
854 crustal reservoir thought to be due to input of mafic magma. As it is this input of mafic
855 magma into the shallow storage system that is thought to have initiated and
856 sustained the five extrusive phases of the Soufriere Hills Volcano (Devine et al.,
857 2003), the implication is that another extrusive phase cannot be ruled out. We
858 conclude that the eruptive sequence of Montserrat's Soufrière Hills volcano is still
859 ongoing with magma trickling into a crustal reservoir. It remains an open question if
860 there is enough crystal-poor, melt-rich, eruptible magma that could reach the surface
861 in the near future. To evaluate the near-term threat for Montserrat the crucial problem
862 needs to be addressed why a new phase started in the past, when it started.
863 Processes like segregation and turnover processes in a crustal reservoir of melt and
864 crystal mush might hold the answer but are far from being understood. It also points
865 to the need for continued close monitoring of the volcano to identify any signs of the
866 beginning of a new phase of extrusion as early as possible.

867

868 **Acknowledgements**

869 Thanks to the staff of the MVO who continuously monitor and assess the risk posed by the
870 Soufrière Hills Volcano for access to the unique data explored in this study. We also thank
871 them for contributions and insights shared during discussions with the Scientific Advisory
872 Committee (SAC) which generated many of the ideas explored in this manuscript. We would
873 like to acknowledge further contributions by SAC members Jenni Barclay, Eleonora Rivalta,
874 and Fidel Costa, and thank Luca Caricchi for insightful discussions. The comments of two
875 reviewers that improved the manuscript are highly appreciated. This research was supported
876 by the Earth Observatory of Singapore via its funding from the National Research
877 Foundation Singapore and the Singapore Ministry of Education under the Research Centres

878 of Excellence initiative. This work comprises EOS contribution number 433. JN is partly
879 funded by NERC Centre for the Observation and Modelling of Earthquakes, Volcanoes and
880 Tectonics (COMET).

881

882 **References**

883 Caricchi, L. & Simpson, G. 2015. Assessment of potential effect of degassing on the
884 deformation observed at Soufriere Hills Montserrat since 1995. Appendix 10 in: 20th Report
885 of the Scientific Advisory Committee on Montserrat Volcanic Activity. <http://www.mvo.ms/>

886 Christopher, T.E., Blundy, J., Cashman, K., Cole, P., Edmonds, M., Smith, P.J., Sparks,
887 R.S.J., Stinton, A. 2015. Crustal-scale degassing due to magma system destabilization and
888 magma-gas decoupling at Soufrière Hills Volcano, Montserrat. *Geochem. Geophys. Geosys.*,
889 16 (9), 2797-2811. doi:10.1002/2015GC005791.

890 Del Negro, C., Currenti, G., Scandura, D. 2009. Temperature-dependent viscoelastic
891 modeling of ground deformation: Applications to Etna volcano during the 1993-1997 inflation
892 period. *Phys. Earth. Planet. Inter.*, 172 (3-4), 299-309. doi:10.1016/j.pepi.2008.10.019.

893 Devine, J.D., Rutherford, M.J., Norton, G.J. & Young, S.R. 2003. Magma storage region
894 processes inferred from geochemistry of Fe-Ti oxides in andesitic magma, Soufrière Hills
895 volcano, Montserrat, WI. *Journal of Petrology*, 44,1375-1400.

896 Dieterich, J.H., Decker, R.W. 1975. Finite element modelling of surface deformation
897 associated with volcanism, *J. Geophys. Res. Solid Earth*, 80, 4096-4102, doi
898 10.1029/JB080i029p04094.

899 Edmonds, M., Pyle, D.M., Oppenheimer, C. 2001. A model for degassing at Soufrière Hills
900 Volcano, Montserrat, West Indies, based on geochemical data. *Earth. Planet. Sci. Lett.*, 186
901 (2) 159-173. doi: 10.1016/s0012-821X(01)00242-4.

902 Edmonds, M., Pyle, D.M., Oppenheimer, C. 2002. HCl emissions at Soufrière Hills Volcano,
903 Montserrat, West Indies, during a second phase of dome building: November 1999 to
904 October 2000. *Bull. Volcanol.*, 64 (1), 21-30. doi: 10.1007/s00445-001-0175-0.

905 Edmonds, M., Humphreys, M.C.S., Hauri, E.H., Herd, R.A., Wadge, G., Rawson, H.,
906 Ledden, R., Plail, M., Barclay, J., Aiuppa, A., Christopher, T.E., Giudice, G., Guida, R. 2014.
907 Pre-eruptive vapour and its role in controlling eruption style and longevity at Soufrière Hills
908 Volcano. In: Wadge, G., Robertson, R.E.A., Voight, B. (Eds.). *The Eruption of Soufrière Hills
909 Volcano, Montserrat from 2000 to 2010. Mem. Geol. Soc. Lond.*, 39, 291-315.
910 doi:10.1144/M39.16.

911 Elsworth, D., Mattioli, G., Taron, J., Voight, B., Herd, R. 2008. Implications of magma
912 transfer between multiple reservoirs on eruption cycling. *Science*, 322 (5899), 246-248.
913 doi:10.1126/science.1161297.

914 Elsworth, D., Foroozan, R., Taron, J., Mattioli, G.S., Voight, B. 2014. Geodetic imaging of
915 magma migration at Soufrière Hills Volcano 1995 to 2008. In: Wadge, G., Robertson, R.E.A.,
916 Voight, B. (Eds.). *The Eruption of Soufrière Hills Volcano, Montserrat from 2000 to 2010.
917 Mem. Geol. Soc. Lond.*, 39, 219-227. doi:10.1144/M39.12.

918 Feuillet, N., Leclerc, F., Tapponnier, P., Beauducel, F., Boudon, G., Le Friant, A., Deplus, C.,
919 Lebrun, J-F., Nercessian, A., Saurel, J-M., Clément, V. 2010. Active fault induced by slip
920 partitioning in Montserrat and link with volcanic activity: New insights from the 2009
921 GWADASEIS marine cruise data. *Geophys. Res. Lett.*, 37 (19), L00E15. doi:
922 10.1029/2010GL042556.

923 Foroozan, R., Elsworth, D., Voight, B., Mattioli, G.S. 2010. Dual reservoir structure at
924 Soufrière Hills Volcano inferred from continuous GPS observations and heterogeneous
925 elastic modeling. *Geophys. Res. Lett.*, 37 (19), L00E12. doi:10.1029/2010GL042511.

926 Foroozan, R., Elsworth, D., Voight, B., Mattioli, G.S. 2011. Magmatic-metering controls the
927 stopping and restarting of eruptions. *Geophys. Res. Lett.*, 38 (5), L05306.
928 doi:10.1029/2010GL046591.

929 Gottsmann, J., Odbert, H. 2014. The effects of thermomechanical heterogeneities in island
930 arc crust on time-dependent preeruptive stresses and the failure of an andesitic reservoir. *J.*
931 *Geophys. Res. Solid Earth*, 119, 4626-4639, doi:10.1002/2014JB011079.

932 Gudmundsson, A. 1990. Emplacement of dikes, sills and crustal magma chambers at
933 divergent plate boundaries. *Tectonophysics*, 176(3-4), 257–275. [https://doi.org/10.1016/0040-](https://doi.org/10.1016/0040-1951(90)90073-H)
934 1951(90)90073-H

935 Hautmann, S., Gottsmann, J., Sparks, R.S.J., Mattioli, G.S., Sacks, I.S., Strutt, M.H. 2010.
936 Effect of mechanical heterogeneity in arc crust on volcano deformation with application to
937 Soufrière Hills volcano, Montserrat, West Indies. *J. Geophys. Res., Solid Earth*, 115 (B9).
938 doi:10.1029/2009JB006909.

939 Hautmann, S., Witham, F., Christopher, T., Cole, P., Linde, A.T., Sacks, I.S., Sparks, R.S.J.
940 2014. Strain field analysis on Montserrat (W.I.) as tool for assessing permeable flow paths in
941 the magmatic system of Soufrière Hills Volcano. *Geochem. Geophys. Geosys.*, 15, 676-690,
942 doi:10.1002/2013GC005087.

943 Head, M., Hickey, J., Gottsmann, J., Fournier, N. 2019. The influence of viscoelastic crustal
944 rheologies on volcanic ground deformation: Insights from models of pressure and volume
945 change. *J. Geophys. Res. Solid Earth*, 124, 8127–8146. doi:10.1029/2019JB017832

946 Herring, T. A., King, R.W., McClusky, S. C. 2010a. GAMIT: GPS Analysis at MIT Release
947 10.4, Internal Memorandum. Massachusetts Institute of Technology, Cambridge, MA.

948 Herring, T.A., King, R.W., McClusky, S. C. 2010b. GLOBK: Global Kalman filter VLBI and
949 GPS Analysis Program Release 10.4, Internal Memorandum. Massachusetts Institute of
950 Technology, Cambridge, MA.

951 Hickey, J., Gottsmann, J., Nakamichi, H., & Iguchi, M. 2016. Thermomechanical controls on
952 magma supply and volcanic deformation: Application to Aira caldera, Japan. *Scientific*
953 *Reports*, 6(1), 32691. <https://doi.org/10.1038/srep32691>

954 Huppert, H.E., Woods, A.W. 2002. The role of volatiles in magma chamber dynamics.
955 *Nature*, 420, 493-495. doi:10.1038/nature01211.

956 Kokelaar, B.P. 2002. Setting, chronology and consequences of the eruption of Soufrière Hills
957 Volcano, Montserrat (1995-1999). In: Druitt, T.H., Kokelaar, B.P. (Eds). *The Eruption of*
958 *Soufrière Hills Volcano, Montserrat, from 1995 to 1999*. *Mem. Geol. Soc. Lond.*, 21, 1-21.
959 doi:10.1144/GSL.MEM.2002.021.01.02.

960 Le Mével, H., Gregg, P. M., & Feigl, K. L. 2016. Magma injection into a long-lived reservoir to
961 explain geodetically measured uplift: Application to the 2007–2014 unrest episode at Laguna
962 del Maule volcanic field, Chile. *J. Geophys. Res. Solid Earth*, 121, 6092–6108.
963 <https://doi.org/10.1002/2016JB013066>

964 Lin, C.-Y. 2020 Alternative Form of Standard Linear Solid Model for Characterizing Stress
965 Relaxation and Creep: Including a Novel Parameter for Quantifying the Ratio of Fluids to
966 Solids of a Viscoelastic Solid. *Front. Mater.* 7:11. doi: 10.3389/fmats.2020.00011

967 Lopez, A.M., Stein, S., Dixon, T., Sella, G., Calais, E., Jansma, P., Weber, J., & LaFemina,
968 P. 2006. Is there a northern Lesser Antilles forearc block?, *Geophys. Res. Lett.* 33, 7,
969 doi.org/10.1029/2005GL025293

970 Manga M., Hornbach M.J., Le Friant A., Ishizuka O., Stroncik N., Adachi T., Aljahdali M.,
971 Boudon G., Breitzkreuz C., Fraass A., Fujinawa A., Hatfield R., Jutzeler M., Kataoka K.,
972 Lafuerza S., Maeno F., Martinez-Colon M., McCanta M., Morgan S., Palmer M.R., Saito T.,
973 Slagle A., Stinton A.J., Subramanyam K.S.V., Tamura Y., Talling P.J., Villemant B., Wall-
974 Palmer D., Wang F. 2012. Heat flow in the Lesser Antilles island arc and adjacent back arc
975 Grenada basin, *Geochem. Geophys. Geosyst.*, 13, Q08007, doi:10.1029/2012GC004260.

976 Mattioli, G.S., Herd, R.A., Strutt, M.H., Ryan, G., Widiwijayanti, C., Voight, B. 2010. Long
977 term surface deformation of Soufrière Hills Volcano, Montserrat from GPS geodesy:
978 Inferences from simple elastic inverse models. *Geophys. Res. Lett.*, 37 (19) (L00E13).
979 doi:10.1029/2009GL042268.

980 Marsden, L.H., Neuberg, J.W., Thomas, M.E. 2019. Topography and Tilt at Volcanoes.
981 *Frontiers in Earth Science*. 7, doi:10.3389/feart.2019.00317.

982 McGee, L., Reagan, M., Handley, H., Turner, S., Sparks, R.S., Berlo, K., Barclay, J., Turner,
983 M. 2019. Volatile behaviour in the 1995-2010 eruption of the Soufrière Hills Volcano,
984 Montserrat recorded by U-series disequilibria in mafic enclaves and andesite host, *Earth and*
985 *Planetary Science Letters*, 524, 115730.

986 McTigue, D.F. 1987. Elastic stress and deformation near a finite spherical magma body:
987 Resolution of the point source paradox. *J. Geophys. Res.*, 92 (B12), 12931-12940.
988 doi:10.1029/JB092iB12p12931.

989 Mogi, K. 1958. Relations between the Eruptions of Various Volcanoes and the Deformation
990 of the Ground Surfaces around them. *B. Earthq. Res. I. Tokyo.*, 36, 99-134.

991 Morales Rivera, A. M., Amelung, F., Albino, F., Gregg, P. M. 2019. Impact of crustal
992 rheology on temperature-dependent viscoelastic models of volcano deformation: Application
993 to Taal volcano, Philippines. *J. Geophys. Res. Solid Earth*, 124, 978–994.
994 <https://doi.org/10.1029/2018JB016054>

995 Neuberg, J., O’Gorman, C. 2002. A model of the seismic wavefield in gas-charged magma:
996 application to Soufrière Hills Volcano, Montserrat. *Mem. Geol. Soc. Lond.*, 21, 603-609. doi:
997 10.1144/GSL.MEM.2002.021.01.29.

998 Odbert, H., Taisne, B., Gottsmann, J. 2015. Deposit loading and its effect on co-eruptive
999 volcano deformation. *Earth. Planet. Sci. Lett.*, 413, 186-196. doi:
1000 10.1016/j.epsl.2015.01.005.

- 1001 Okada, Y. 1985. Surface deformation due to shear and tensile faults in a half-space. Bull.
1002 Seismol. Soc. Am., 75 (4), 1135-1154.
- 1003 Okada, Y. 1992. Internal deformation due to shear and tensile faults in a half-space. Bull.
1004 Seismol. Soc. Am., 82 (2), 1018-1040.
- 1005 Paulatto, M. 2011. Probing the interior of an active volcano: Three-dimensional seismic
1006 tomography at Montserrat, School of Ocean and Earth Science, University of Southampton,
1007 PhD thesis, pp. 261.
- 1008 Paulatto, M., Moorkamp, M., Hautmann, S., Hooft, E., Morgan, J. V., Sparks, R. S. J. 2019.
1009 Vertically extensive magma reservoir revealed from joint inversion and quantitative
1010 interpretation of seismic and gravity data. J. Geophys. Res. Solid Earth, 124, 11,170–
1011 11,191. <https://doi.org/10.1029/2019JB018476>
- 1012 Ryan, G. A., Shalev, E. 2014, Seismic Velocity/Temperature Correlations and a Possible
1013 New Geothermometer: Insights from Exploration of a High-Temperature Geothermal System
1014 on Montserrat, West Indies: Energies, 7, 6689-6720.
- 1015 Segall, P. 2010. Earthquake and Volcano Deformation. Princeton, N.J.: Princeton University
1016 Press, p.213.
- 1017 Segall, P. 2016. Repressurization following eruption from a magma chamber with a
1018 viscoelastic aureole. J. Geophys. Res. Solid Earth, 121, 8501-8522,
1019 doi:10.1002/2016JB013597.
- 1020 Stinton, A.J., Cole, P.D., Stewart, R.C., Odbert, H.M., Smith, P. 2014. The 11 February 2010
1021 partial dome collapse at Soufrière Hills Volcano, Montserrat. In: Wadge, D., Robertson,
1022 R.E.A., Voight, B. (Eds.). The Eruption of Soufrière Hills Volcano, Montserrat from 2000 to
1023 2010. Mem. Geol. Soc. Lond., 39, 133-152. doi:10.1144/M39.7.

1024 Stinton, A.J., Bass, V., Christopher, C., Fergus, M., Miller, V., Pascal, K., Rostant, D., Ryan,
1025 G.A., Stewart, R., Syers, R., Wade, V., Williams, P. 2020. MVO Open File Report OFR 20-
1026 01. Montserrat Volcano Observatory, Flemmings, Montserrat.

1027 Voight, B., Widiwijayanti, C., Mattioli, G., Elsworth, D., Hidayat, D., Strutt, M. 2010. Magma-
1028 sponge hypothesis and stratovolcanoes: Case for a compressible reservoir and quasi-steady
1029 deep influx at Soufrière Hills Volcano, Montserrat. *Geophys. Res. Lett.*, 37 (19).
1030 doi:10.1029/2009GL041732.

1031 Wadge, G., Herd, R., Ryan, G., Calder, E.S., Komorowski, J.-C. 2010. Lava production at
1032 Soufrière Hills Volcano, Montserrat: 1995-2009. *Geophys. Res. Lett.*, 37(19), L00E03.
1033 doi:10.1029/2009GL041466.

1034 Wadge, G., & Aspinall, W.P. 2014. A review of volcanic risk-assessment praxis at the
1035 Soufrière Hills volcano from 1997 to 2011, In: Wadge, D., Robertson, R.E.A., Voight, B.
1036 (Eds.). *The Eruption of Soufrière Hills Volcano, Montserrat from 2000 to 2010. Mem. Geol.*
1037 *Soc. Lond.*, 39, 1-40. doi:10.1144/M39.24.

1038 Wadge, G., Voight, B., Sparks, R.S.J., Cole, P.D., Loughlin, S.C., Robertson, R.E.A. 2014.
1039 An overview of the eruption of Soufrière Hills Volcano, Montserrat from 2000 to 2010. In:
1040 Wadge, D., Robertson, R.E.A., Voight, B. (Eds.). *The Eruption of Soufrière Hills Volcano,*
1041 *Montserrat from 2000 to 2010. Mem. Geol. Soc. Lond.*, 39, 1-40. doi:10.1144/M39.1.

1042 Watts, R.B., Herd, R.A., Sparks, R.S.J., Young, S.R. 2002. Growth patterns and
1043 emplacement of the andesitic laval dome at Soufrière Hills Volcano, Montserrat. In: Druitt,
1044 T.H., Kokelaar, B.P. (Eds). *The Eruption of Soufrière Hills Volcano, Montserrat, from 1995 to*
1045 *1999. Mem. Geol. Soc. Lond.*, 21, 115-152. doi:10.1144/GSL.MEM.2002.021.01.06.

1046 Yamasaki, T., Kobayashi T., Wright, T.J., Fukahata, Y. 2017. Viscoelastic crustal
1047 deformation by magmatic intrusion: A case study in the Kutcharo caldera, eastern Hokkaido,
1048 Japan., *J. Volc. Geotherm. Res.*, 349 128-145. doi.org/10.1016/j.jvolgeores.2017.10.011

1049 Zellmer, G.F., Sparks, R.S., Hawksworth, C.J., Wiedenbeck, M. 2003. Magma emplacement
1050 and remobilization timescales beneath Montserrat: Insights from Sr and Ba profiles across
1051 plagioclase phenocrysts. *J. Petr.*, 44, 1413-1432.